Atomistic simulations of copper oxidation and Cu/Cu_{2}O interfaces using charge-optimized many-body potentials

Bryce Devine, Tzu-Ray Shan (單子睿), Yu-Ting Cheng (鄭鈺婷), Alan J. H. McGaughey, Minyoung Lee, Simon R. Phillpot, and Susan B. Sinnott

Atomistic Simulations of Copper Oxidation and Cu₂O Interfaces using COMB Potentials

Bryce Devine[1], Tzu-Ray Shan(單子睿)[1], Yu-Ting Cheng(鄭宇庭)[1], Alan J. H. McGaughey[1,2],

Minyoung Lee[2], Simon R. Phillpot[1], and Susan B. Sinnott[1*]

[1] Department of Materials Science and Engineering, University of Florida,

Gainesville, FL 32611-6400, USA

[2] Department of Mechanical Engineering, Carnegie-Mellon University,

Pittsburgh, PA, 15213, USA

*Author to whom correspondence should be addressed. Email: ssinn@mse.ufl.edu

ABSTRACT

Presented is a charge optimized many body potential (COMB) for metallic copper and copper

oxide systems based on an extended Tersoff formalism coupled with variable charge

electrostatics. To faithfully reproduce interactions between molecular oxygen and the metal

surface, the potential includes atomic polarizabilities via both a point dipole model and dynamic

partial charges, both of which are equilibrated through an extended Lagrangian scheme. The

potential is fit to a training set composed of both experimental and *ab initio* computational data

for cohesive energies, formation enthalpies, elastic properties and surface energies of several

metallic and oxide phases as well as bond dissociation energies for molecular oxygen and several

of its anions. The potential is used in molecular dynamics simulations to model the

$Cu(111)\|Cu_2O(100)$ interface and the oxidation of the $Cu(100)$ surface.

KEYWORDS: Copper, Copper Oxide, Oxidation, Empirical Potential, Charge Transfer, Variable

Charge, Charge Optimized Potential, COMB, Molecular Dynamics Simulations

1. Introduction

Historically, copper has been used as a model system for the fundamental study of early stage oxidation and oxide film growth of transition metal surfaces.[1-7] Notable studies of copper oxidation have been published over the past six decades since copper was included in the original work of Cabrera and Mott.[8] General findings that are consistent throughout a range of studies indicate that oxidation proceeds from chemisorption of atomic oxygen to the formation of an oxygen deficient induction layer that facilitates the growth of three-dimensional Cu_2O islands.[6, 9-11] While the current body of experimental work strongly supports a heteroepitaxial growth model which rate is limited by oxygen surface diffusion,[6, 10, 12] the details of the metal/oxide morphology are somewhat contradictory in the literature. For instance, *in situ* transmission electron microscopy (TEM) experiments indicate a correlation between island nucleation and step edges.[3, 13] However, a more recent study conducted at higher resolution found a more significant increase in growth rates at grain boundaries.[14, 15] Diffraction and electron microscopy observations consistently indicate that Cu_2O islands form with the [110] plane of the oxide at the interface regardless of the structure of the metal surface upon which it forms.[2, 3] Epitaxial growth oriented along the (110) direction of the metal is preferred.[2, 3] While the termination of the oxide is invariant with the metal surface, the shape of the islands does vary among copper surfaces.[3] More recently, *in situ* TEM experiments indicate that island morphology also varies with reaction temperature.[12, 15]

This leads to the promising possibility that if the mechanism of oxidation can be resolved to the point where the dependence of island morphology on reaction conditions is understood at the atomic scale, controlled oxidation could be used as a means to direct the morphology of engineered oxide nano-structures. Resolving the oxidation mechanism requires a theoretical

method with the fidelity and capability of efficiently modeling the structures of interest. One choice is an empirical potential that can be incorporated into a molecular dynamics (MD) or kinetic Monte Carlo scheme. First principles methods, such as density functional theory (DFT), have the highest fidelity currently available but are limited by both the size and the time scale of the problem. Because oxide formation is a diffusion limited process that is influenced by strains at the interface,[6] atomic-scale simulation of the formation of a single small island involves tens of thousands of atoms, which exceeds the current capacity of traditional DFT methods by at least an order of magnitude. Hence, to enable the study of oxidation on a meaningful length scale, high-fidelity analytical interatomic potentials must be used.

In this work, we develop an interatomic potential suitable for modeling metallic Cu, Cu oxide phases and interfaces between Cu and Cu oxides, as well as for carrying out large scale Cu oxidation simulations.

2. Methodology

2.1 Modeling Cu oxidation and Cu oxides

Copper forms pertinent oxides in two different oxidations states. Oxide islands and the initial oxide layer formed during oxidation of metallic copper are composed of cuprous oxide (Cu_2O), which is cubic with space group $Pn\bar{3}m$ (see Fig.1A).[16] The structure can be viewed as a face centered cubic (FCC) lattice of cations, with anions occupying ¼ of the tetrahedral sites at positions (1/4,1/4,1/4) and (3/4,3/4,3/4), or as a body centered cubic (BCC) lattice of anions with cations occupying one half of the (1/4,1/4,1/4) positions. This results in two-fold coordination around each cation with a linear O-Cu-O bond angle. As oxidation proceeds, the oxide phase

4

converts to the monoclinic cupric oxide, CuO, that has space group, *C2/c* (see Fig.1B).[17] The linear O-Cu-O bond persists in the higher oxide although the cation is now four-fold coordinated.

Simulations of oxide formation naturally fall under the scope of variable charge potentials that can simultaneously model the oxygen molecule, a metallic solid, and the evolving stoichiometry of the oxide as growth progresses. In choosing a potential form for a metal/metal oxide system, a good first guess would be along the lines of an embedded atom method (EAM)[18] or second moment based potential such as Finnis-Sinclair[19] coupled with an electrostatic model. This approach was pursued by Streitz and Mintmire with their electrostatics+ (ES+) model for aluminum and alumina systems,[20] which coupled a variable charge electrostatic scheme to a Finnis-Sinclair bond order potential. The ES+ model has subsequently been extended with some refinement to several additional oxide and alloy systems.[14, 15]

However, the significant directionality in the bonding for the most relevant Cu oxide phases requires a potential optimized for covalent interactions, such as the Tersoff's potential.[21, 22] Several recently published potentials link variable charge (QEq) electrostatics with extended Tersoff type potentials. For example, Yasukawa *et al.* developed one such potential for the covalent Si-SiO$_2$ system.[23] This potential was later refined by Yu *et al.* in their Charge Optimized Many Body (first-generation COMB) potential to reproduce the SiO$_2$ phase order[24] and by Shan *et al.* in their second-generation COMB potential for SiO$_2$ and amorphous silica.[25] The ReaxFF family of force fields employs a similar bond order dependent approach and has been adapted to several metal-oxide systems[26-28] and most recently Cu/Cu$_2$O/water interactions.[29] A significant concern with using a bond-order based potential is its applicability to close-packed metals. However, as shown by Brenner, the functional form of Tersoff's bond order potential is algebraically similar to the Finnis-Sinclair's potential with the addition of an angular dependence

in the bond order term.[30] The applicability of this potential form to model metallic systems was demonstrated by Iwasaki *et al.*, who extended Yasukawa's potential to several metallic systems[31-33] and, more recently, by Yu *et al.* who developed a modified form of Yasukawa's potential for metallic copper based on Iwasaki's parameterizations.[34] In this work, we start with the second-generation COMB potentials, and Yu's and Iwasaki's parameterizations provide a starting point from which to develop an analytical potential for the copper oxide phases.

2.2 A dynamic charge electrostatic energy function

The electron density, $\rho(\mathbf{r})$, at each site, i, of a collection of ions exhibits a chemical potential, μ_i, that has been shown to be equivalent to the partial derivative of the energy, U, with respect to density: $\partial U/\partial\rho(\mathbf{r})$.[35] By this definition, μ_i is equivalent to the negative of the electronegativity, x_i at each site. The principle of electronegativity equilibration (EE), states that in a closed system of interacting ions at chemical equilibrium, the electron density is distributed such that the electrochemical potential and hence the electronegativity is equal at all sites.[35] With the additional approximation that atomic charges occupy a fixed volume around each atom, μ_i can be defined as the partial derivative of energy with respect to partial charge: $\partial U/\partial q_i$, where q_i is the partial charge of atom i. The partial charge on each atom can be determined as that which corresponds to the equilibrium electronegativity.

Determination of the equilibrium partial charges through the EE method requires an optimization of N variables for each change in the atomic positions, where N is the number of atoms in equilibrium. This is the most computationally burdensome portion of the method; Shan has shown that charge equilibration of COMB potentials usually takes as many as 80% of the computational time.[36] For efficiency and extensibility to larger system sizes, we use a simulated

6

annealing technique. We make the charge and position of each atom dependent upon time and

apply the Lagrangian introduced by Rick et al. [36]

$$L = \sum_{i=1}^{N} \frac{1}{2} m_i \dot{r_i}^2 + \sum_{i=1}^{N} \frac{1}{2} M_Q \dot{q_i}^2 - U[\{q\};\{\mathbf{r}\}] - v \sum_{i=1}^{N} q_i \qquad . \tag{1}$$

m_i, r_i and q_i correspond to the mass, position and charge of atom i respectively. M_Q is a fictitious

charge mass. v is an undetermined multiplier that enforces the constraint that charge in the

system is conserved. The potential energy, U[q,$\mathbf{r}$] is defined for a collection of ions, where q and

$\mathbf{r}$ represent the set of atomic charges and positions. The evolution in time of the atomic positions

and charges are given by the following equations of motion:

$$m_i \ddot{r_i} = \frac{\partial U[\{q\};\{\mathbf{r}\}]}{\partial r_i} \qquad . \tag{2}$$

$$M_Q \ddot{q_i} = \frac{\partial U[\{q\};\{\mathbf{r}\}]}{\partial q_i} - v_i \qquad . \tag{3}$$

v is shown by Rick to be equal to the mean electronegativity and, when substituted in Eq. 4,

gives:

$$M_Q \ddot{q_i} = \chi_i - \bar{\chi_i} \qquad . \tag{4}$$

The partial charge on each atom is determined by iteratively solving the equations of

motion with damping for each set of nuclear positions until the electronegativity, χ_i, on each

atom is sufficiently close to the mean electronegativity, $\bar{\chi_i}$, of the system. The tolerance, usually

$10^{-3} \sim 10^{-5}$, used to determine whether the energy is minimized with respect to partial charges is

optimized to ensure energy conservation over the time span of the simulation. Compared to the

traditional method of solving the charges via a self-consistent loop at each MD step, the

Lagrangian method employed in this work does not involve taking the inverse of an N by N

matrix. While the Lagrangian method includes fictitious charge mass and charge time-step and an arbitrary damping factor, it has better efficiency for scaling with N. The optimized charge mass and time-step is 5.4858×10^{-4} amu and 0.0005 fs, respectively, and the damping is chosen to be 0.05.

The total potential energy function is composed of the electrostatic energy, U^{es} and a short range bond energy U^{bond}. The bond energy is composed of the pair sum over an analytical potential, $V^{Bond}(r_{ij,})$, which will be described in the next section. The electrostatic energy for a systems of rigid atom centered charge density distributions includes the energy to form a charge on each atom, $V^{Self}(q_i)$, and the Coulombic interaction between charges densities. For convenience, we make use of Streitz and Mintmire's rigid density distribution functions where the density is a function of position, **r,** and charge:

$$\rho_i(\mathbf{r};q_i) = Z_i \delta(|\mathbf{r} - \mathbf{r_i}|) + (q_i - Z_i) f_i(|\mathbf{r} - \mathbf{r_i}|) \quad , \tag{5}$$

$$f(|\mathbf{r} - \mathbf{r_i}|) = \xi_i^3 \pi^{-1} \exp(-2\xi_i |\mathbf{r} - \mathbf{r_i}|) \quad . \tag{6}$$

Here, Z_i is an effective point core charge treated as a fitted parameter. δ is the Kronecker delta function. $f(\mathbf{r})$ is a function that describes the radial decay of the charge density, where ξ is an orbital exponent that controls the rate of decay. Integration over electron densities between pairs of atoms yields for the total electrostatic energy:

$$U^{es}[\{q\};\{\mathbf{r}\}] = \sum_i V_i^{Self}(q) + \tfrac{1}{2}\sum_i\sum_{j \neq i} q_i J_{ij}^{qq} q_j + \sum_i\sum_{j \neq i} q_i J_{ij}^{qz} Z_j \quad , \tag{7}$$

J^{qq} is the pairwise interaction between charge densities defined as the Coulomb integral:

$$J_{ij}^{qq} = [\rho_i | \rho_j] = \int d^3 r_1 \int d^3 r_2 \frac{\rho_i(\mathbf{r}_1)\rho_j(\mathbf{r}_2)}{r_{12}} \quad , \tag{8}$$

where, $\mathbf{r}_1$ and $\mathbf{r}_2$ indicate the centers of $\rho_i(\mathbf{r})$ and $\rho_j(\mathbf{r})$. r_{12} is the distance between density distributions. The charge-nuclear coupling operator, J_{ij}^{qZ}, in Eq. 7 is equal to a shielded nuclear attraction integral:

$$J_{ij}^{qZ} = \left[j | \rho_i \right] - \left[\rho_j | \rho_i \right] \qquad , \qquad (9)$$

$$\left[j | \rho_i \right] = \int d^3 r \, \frac{\rho_i(\mathbf{r})}{|\mathbf{r} - \mathbf{r}_i|} \qquad . \qquad (10)$$

As indicated in Eq. 7, the interactions between point core charges are not explicitly determined, but instead are assumed to be included in bond energy, $V^{Bond}(r_{ij})$ along with all non-electrostatic energy contributions.

For the self energy, V^{Self}, we begin with the approach of Rappe and Goddard,[37] where the energy of a neutral atom as a function of charge may be expanded as a Taylor series:

$$V_i^{Self}(q_i) = E_i^0(0) + \chi_i q_i + J_{ii} q_i^2 + K_i q_i^3 + L_i q_i^4 + ... \qquad (11)$$

$E^0(0)$ is the ground state energy of a free atom. χ_i and J_{ii} can be thought of as the one centered integrals of the form $[i | \rho_i]$ and $[\rho_i | \rho_j]$, in which case they represent the self interaction potential on each atom, i. The values for coefficients in Eq. 11 are treated as atom specific parameters and are determined by fitting to gas phase ionization potentials and electron affinities for each atom.

The pair interaction described by Eq. 8 includes an r^{-1} term, which is solved via a direct Wolf summation[38] that is spherically truncated after 11Å. This adds an additional function of q^2 to the self energy, which is included implicitly in the fitted atomic coefficient, J_{ii}. In second-generation COMB potentials[25, 39], the self energy contribution from the direct summation was considered extraneous from the potential. In those cases, when atoms interact, the contribution to the self energy from the Wolf summation shifts the effective atomic ionization potential and

electron affinities away from values of isolated atoms. By including all self energy contributions in V^{self}, the atomic ionization energies are consistent between interacting and non-interacting atoms and are consistent with calculated reference values.

2.3 The charge dependent bond order potential.

This work follows the Yasukawa formalism, where, with non charged atoms, the short range potential, $V^{Bond}(r_{ij})$, is equivalent to Tersoff's bond order potential. The bond energy is described with a repulsive, V^R, and attractive, V^A, exponential functions of bond length, r_{ij}. The Yasukawa potential deviates from Tersoff in that the magnitude and radial decay of the pair interactions vary with charge. Charge dependent correction functions, $D_i(q_i)$, are added to the exponential coefficient of the short range energies to reflect the change in atomic radius with charge.

$$V^R(r_{ij}, q_i, q_j) = F_c(r_{ij}) A_{ij} \exp\left\{-\lambda_{ij} r_{ij} + \tfrac{1}{2}\left[\lambda_i D_i(q_i) + \lambda_j D_j(q_j)\right]\right\} \quad , \tag{13}$$

$$V^A(r_{ij}) = F_c(r_{ij}) b_{ij} B_{ij} B_{ij}^*(q_i, q_j) \exp\left\{-\alpha_{ij} r_{ij} + \tfrac{1}{2}\left[\alpha_i D_i(q_i) + \alpha_j D_j(q_j)\right]\right\} \quad . \tag{14}$$

Here A_{ij}, B_{ij}, λ_{ij} and α_{ij} are parameters that are determined for each bond type. The change in short range contributions, $D_i(q_i)$, is specific to each element type. In particular,

$$D_i(q_i) = D_{U_i} + \left|b_{D_i}\left(Q_{U_i} - q_i\right)\right|^{n_{D_i}} \quad , \tag{15}$$

$$b_{D_i} = \left(D_{L_i} - D_{U_i}\right)^{\frac{1}{n_{D_i}}} \Big/ \left(Q_{U_i} - Q_{L_i}\right) \quad , \tag{16}$$

$$n_{D_i} = \frac{\ln D_{U_i} - \ln(D_{U_i} - D_{L_i})}{\ln Q_{U_i} - \ln(Q_{U_i} - Q_{L_i})} \quad , \tag{17}$$

and D_U and D_L are parameters that reflect the change in atomic radius with charge. Likewise, Q_U and Q_L are the atomic charges that correspond to the limits of the valence shell.

Additionally, the bond energy is scaled with a charge dependent function $B_{ij}^{*}(q_i,q_j)$ that reflects the change in bond order with charge:

$$B_{ij}^{*}(q_i,q_j) = \left(B_i^{*}B_j^{*}\right)^{\frac{1}{2}} \qquad , \qquad (18)$$

$$B_i^{*} = \left[a_{B_i} - \left| b_{B_i}\left(q_i - Q_{O_i}\right)\right|^{n_{B_i}} \right] \qquad , \qquad (19)$$

$$b_{B_i} = \frac{\left|a_{B_i}\right|^{\frac{1}{n_{B_i}}}}{\Delta Q_i} \qquad , \qquad (20)$$

$$a_{B_i} = \left(1 - \left|\frac{Q_{O_i}}{\Delta Q_i}\right|^{n_{B_i}}\right)^{-1} \qquad , \qquad (21)$$

$$\Delta Q_i = \frac{1}{2}\left(Q_{u_i} - Q_{L_i}\right) \qquad , \qquad (22)$$

$$Q_{O_i} = \frac{1}{2}\left(Q_{u_i} + Q_{L_i}\right) \qquad . \qquad (23)$$

n_{Bi} is a fitted parameter. In Eq. 14, b_{ij}, is Tersoff's bond order term that modifies the short range attraction contribution based on bond angles, local symmetry and number of nearest neighbors:

$$b_{ij} = \left[1 + \left(\beta_i \sum_{j\neq i}^{N}\sum_{k\neq i,j}^{N}\zeta_{ijk}(r_{ij},r_{ik})g(\theta_{ijk})\right)^{\eta_i}\right]^{\frac{-1}{2\eta_i}} \qquad , \qquad (24)$$

$$\zeta_{ijk} = F_c(r_{ik})\exp\left[a_{ij}^{m_i}\left(r_{ij} - r_{ik}\right)^{m_i}\right] \qquad , \qquad (25)$$

$$g(\theta_{ijk}) = 1 + \frac{c_{ij}^2}{d_{ij}^2} - \frac{c_{ij}^2}{d_{ij}^2 + (h_{ij} - \cos\theta_{ijk})^2} \qquad . \qquad (26)$$

a, β, η, m, c, d and h are fitted parameters. The function, $F_c(r_{ij})$ smoothly terminates the short range interactions within a cutoff region defined by two cutoff radii, R_s and S_s:

$$F_C(r_{ij}) = \begin{cases} 1 & r_{ij} \leq R_{S-ij} \\ \dfrac{1}{2}\left[1 + \cos\left(\pi \dfrac{r_{ij} - R_{S-ij}}{S_{S-ij} - R_{S-ij}}\right)\right] & R_{S-ij} < r_{ij} \leq S_{S-ij} \\ 0 & r_{ij} \geq S_{S-ij} \end{cases} \qquad (27)$$

2.4 Charge independent short range energy functions

While the Yasukawa potential and the subsequent COMB formalism can be parameterized to provide a classical approximation of chemical bonding in the ideal ground state structure, we have found it necessary to introduce additional interactions to reproduce the phase order of copper oxide and metallic copper phases, as well as to improve the behavior of molecular oxygen. A similar requirement was found necessary by Yu in the developing the first-generation COMB potential for SiO_2 and Cu.[24, 34]

In the current potential, dependence of the bond energy on bond angle and coordination resides solely in the bond order function that, in turn, gets smaller with increasing charge. This tends to be problematic for copper oxide phases, which exhibit directionality in the bonding in both the Cu(I) and Cu(II) oxides. In both oxides, the O-Cu-O bond angle remains 180° with low coordination around Cu. The bond angle and coordination terms in b_{ij} alone are insufficient to stabilize these structures. An additional charge independent angular function based on the first, second and third order Legendre polynomials summed over the nearest neighbors (NN) is included in the bond energy:

$$V_{ij}^{LP}(\cos\theta_{ijk}) = K_{LP}^1\left(1 + \sum_{j\neq i, k\neq i}^{NN}\cos\theta_{ijk}\right) + K_{LP}^2\left[1 + \tfrac{1}{2}\sum_{j\neq i, k\neq i}^{NN}(3.0\cos^2\theta_{ijk} - 1.0)\right]$$
$$+ K_{LP}^3\left[1 + \tfrac{1}{2}\sum_{j\neq i, k\neq i}^{NN}(5.0\cos^3\theta_{ijk} - 3.0\cos\theta_{ijk})\right] \qquad (28)$$

K_{LP} are fitted parameters specific to the bond type.

The potential overly stabilizes dense oxide phases such as CuO as rocksalt. An additional coordination dependent term is needed to de-stabilize these higher coordination phases. The coordination correction first used in the ReaxFF force field[26, 40] and later adapted by COMB HfO$_2$ potential[39] is also applied here:

$$V_i^{Coord}(\Delta N_i) = E_i^{Coord} \Delta N_i / \left(1 + \exp(\gamma_i^{Coord} \Delta N_i)\right) \qquad , \tag{29}$$

$$\Delta N_i = CN_i - CN_i^* \qquad , \tag{30}$$

$$CN_i = \sum_{j \neq i}^{NN} F_c\left(r_{ij}, R_{s-ij}, S_{s-ij}\right) \qquad . \tag{31}$$

CN^* is the coordination number of the element in the ideal structure, and E^{Coord} and γ_i^{Coord} are fitted parameters. The correction is only applied for Cu-O interactions such that CN_i is the number of Cu-O bonds formed around atom i.

The charge independent correction terms are consistent with the first-generation COMB potentials. Yu's potential for metals includes identical angular functions based on the Legendre polynomials to destabilize the HCP structure relative to FCC in close packed metals. The coordination functions only apply to aberrant dense phases of the oxide and do not contribute to the ground state energy of the oxide phases of interest in this work.

2.5 Parameterization of the potential

The main goal of parameterization is to faithfully reproduce the surface and mechanical properties of the metal and the relative formation enthalpies of accessible oxide phases while maintaining a reliable degree of transferability to possible non-stoichiometric oxides that may arise during oxidation. To ensure transferability, parameters are determined as a weighted least squares best fit to a test set of properties of multiple phases with variation in coordination around the metal. The potential is further validated against an additional set of parameters such as

13

surface energies, defect formation enthalpies and mechanical properties determined with fully relaxed ionic positions.

This potential is an integral part of a family of COMB potentials, which are intended to be compatible with one another. However, in this work, we develop two slightly different parameterizations for the Cu/Cu$_2$O systems. The first set, labeled COMB2010, is based on the Cu potential by Yu *et al.*[24] and is compatible with second-generation COMB potentials[25, 39] and is optimized for interfacial and bulk structures. The second set, labeled COMB2011, is designed to model bulk systems, small molecules, and single atoms in addition to interfaces. So as to provide maximum materials fidelity, a sacrifice to transferability is made in the second parameterization in that parameters for both atomic O and O$_2$ are different from those in first- and second-generation COMB potentials.

To gain maximum flexibility in the parameterization, values are defined based on the interaction type. This is a deviation from the first-generation COMB potentials, where interaction parameters were determined from element specific values via mixing rules.[24] However, in first-generation COMB potentials, correction functions that were specific to the interaction type were added to improve the potential performance. Since any gain in transferability is compromised with the correction terms, there is no perceived benefit in restricting the parameterization to atomic based values. Furthermore, in practice, the mixing rules are found to be insufficient to describe critical interactions. For example, the angular coefficients for metals are very weak in the metallic phase. However, the oxide is characterized by a linear O-Cu-O bond that requires a stronger angular term than what is given by the mixing rules.

2.5.1 Parameterization of atomic and metallic copper

The electrostatic self-energy terms, V^{Self}, for copper are determined as a least squares best fit to the ionization potential and electron affinities determined at the coupled cluster level of theory using singlet and doublet, and perturbative triplet excitations, CCSD(t).[41] A correlation consistent triple zeta basis set (cc-pVTZ)[42] is found to be sufficient to reproduce the first electron affinity and up to the third ionization potential. All *ab initio* calculations are performed with the *Gaussian03* computation suite.[43] When V^{Self} is truncated at the second order, the values may be derived directly from the first ionization potential and electron affinity provided that the energy of the neutral atom is taken as the zero point. However, we have found that higher order terms are required to model energies beyond the first ionization potential, as is necessary for copper with two relevant oxidation states.

The starting point for charge independent parameters are taken from Yu *et al.*,[34] which, in turn, are derived from the Iwasaki potential.[31] The cubic phase of Cu_2O is basically an inter-penetrating network that may be stabilized by covalent Cu-Cu bonding.[44, 45] The Cu-Cu interaction in the oxide requires a longer cutoff than was used by Yu *et al.*, which in turn necessitates a refit of several parameters. The copper parameters at neutral charge are determined as the weighted least squares best fit to experimental cohesive energy and lattice parameter of the FCC ground state. The training data set also includes un-relaxed values for the C_{11}, C_{12} and C_{44} elastic constants, (100), (110) and (111) surface energies and the vacancy formation energy, E_F^V. The energy vs. volume for the FCC ground state as well as the relative energies of the BCC and natural hexagonal close packed (HCP) structures are included in the training data set, as well.

Energy vs. volume curves are calculated with DFT using the *Vienna Ab-Initio Simulation Package ver. 4.6* (*VASP* 4.6).[46] Energies are determined using the projector augmented plane wave method (PAW).[47] The PW91 generalized gradient approximation (GGA) is used for the

exchange and correlation energies. The kinetic energy cutoff is set at 400 eV. Integration over the Brillouin zone is performed over a 10x10x10 Monkhorst-Pack k-point mesh.

The energy vs. volume is calculated over a range of ±5% isometric strain and fit to the Rose equation of state.[48] The resulting equation of state captures the change in energy with volume in which the bulk modulus is constant at each strain point. For fitting purposes, the curves are generated with ionic positions fixed at ideal crystallographic positions, in which case the energy may not be a minimum and the forces may not be zero. The natural equation of state, generated with relaxed ionic positions, is used as a validation on the parameterization. The lattice parameters for higher energy phases that do not appear in the experimental phase diagram are not included in the training set: only their energies relative to the ground state structure are considered. The atomic specific parameters for copper are tabulated in Table 1 and interaction dependent parameters are listed in Table 2A and B. Table 2A lists parameters for COMB2010 and Table 2B lists parameters for COMB2011.

2.5.2 Parameterization of Molecular Oxygen

Oxygen parameters for the self energy function, V^{self}, are determined as a best fit to the ionization potential and to the first and second electron affinities of atomic oxygen calculated at the CCSD(t)/cc-pVTZ level of theory. The O-O interaction parameters are determined as weighted least squares best fit to energy vs. bond length curve for O_2, O_2^{1-} and O_2^{2-} with the intent to capture the bond dissociation energy for the different charge states. Reference data for the energies vs. bond length for the anions are also calculated using coupled cluster theory at the CCSD(t)/cc-pVTZ level. Lastly the polarizability tensor for O_2 and O_2^{1-}, determined via CCSD/cc-pVTZ, are also included in the training data set.

First- and second-generation COMB potentials for oxygen do not reproduce the dissociation behavior of the various anions of O_2, which is because O_2 anions were not included in the training set. The COMB2010 potential, for example, over-stabilizes O_2^{2-} to the point where it is the most stable form of molecular oxygen. This is due to the O^- anion being the lowest energy state of atomic oxygen and the rather large damping of Coulombic interactions at the O_2 bond distance. Our first-principles calculations predict O_2^{2-} to be unstable at any bond length. In order to rectify this deficiency, the predicted dissociation behaviors of the O_2 anions of the COMB2011 potential are corrected with additional electrostatic functions. In particular the potential was expanded to include atomic polarizations via a point dipole model and a correction function that captures the effect of ionic neighbors on the atomic hardness coefficient.

The electronegativity equilibration principle has a well-defined basis in conceptual DFT, which seeks to explain chemical principles that govern reactivity in terms of DFT.[48] While pursuing fundamental definitions for such concepts as electronegativity and chemical hardness, that body of work suggests several improvements to consider in EE based potentials. It has been shown that the self Coulombic coefficient, J_{ii}, is equivalent to the atomic hardness.[49] Conceptual DFT suggests that the atomic hardness describes the Coulombic interaction when an atom is bound within a molecule or embedded in an ionic lattice.[49] In practice, EE methods are parameterized by either fitting the self energy coefficients to atomic gas phase ionization potentials and electron affinities or by fitting to bulk properties. In the former case, the difference between bulk and atomic properties is compensated by other terms within the potential. In COMB2011, we fit to atomic values since we are interested in the interactions involving isolated atoms. To capture the change in atomic hardness as an atom is embedded in the bulk oxide, the

17

hardness coefficient is augmented with a correction function that captures the change with its environment:

$$V_i^{Self}(r_i, q_i) = E_i^0(0) + \chi_i q_i + \left(J_i + \sum_{j \neq i}^{N} F_{ij}^{Field}(r_{ij}, q_j) \right) q_i^2 + K_i q_i^3 + L_i q_i^4 . \tag{32}$$

Following the procedure outlined by Toufar et al.,[50] the environmental effect on the atomic hardness is determined by calculating the atomic self energy at the CCSD(t)/aug-cc-PVTZ level in a symmetric field of point charges. The calculation is performed in a field of eight point charges arranged symmetrically around the atom at varying distance. The idea is to determine the effect of a confining potential on the atomic self energy function. The sum of the charge on the point charges compensates the charge on the central atom such that the net charge of the system remains neutral, thus mimicking charge being transferred from the central atom to its neighbors. The Coulombic interaction between the point charges and the central atom as well as between one another is subtracted from the total energy. Thus any change in the atomic self energy function is due solely to the field effect of the point charges on the atomic self energy. Figure 2 illustrates the calculated field effect of the lattice on the atomic self energy of oxygen and copper. The effect is found to decay with radial distance. A penalty function that captures the change in self energy due to the field strength is fit to the results of the calculation:

$$F_i^{Field}(r_{ij}, q_j) = \frac{1}{4 \pi \varepsilon_o} \sum_{j \neq i}^{NN} \left(\frac{P_1^J q_j}{r_{ij}^3} + \frac{P_2^J q_j^2}{r_{ij}^5} \right) . \tag{33}$$

P_1^J and P_2^J are fitted parameters. The starting point values for oxygen are determined as a least squares best fit to the calculated ionization potential and first and second electron affinities determined in the various fields. These values are refined further along with the other

electrostatic parameters to reproduce the dissociation behavior of O_2 such that the O_2^{-1} anion is lower in energy than the ground state and O_2^{-2} is unstable.

Molecular polarization represents a distortion in the electron density in response to an external electric field. The polarization response can be decomposed into atomic polarization, i.e. contributions due to the distortion of the electron density around each atom, change in the permanent dipole moment of the molecule due to variation in the overlap integrals between bonded atoms and the exchange of charge between bonded atoms.[51] The dynamic charge scheme presented here uses non-polarizable densities, meaning the charge distribution around the atom is fixed relative to the core. As a consequence the charge scheme mimics exchange charge polarization, but does not reproduce atomic polarizations. The calculated polarizability tensor for molecular oxygen is anisotropic. The polarizability along the bond of the molecule is composed of charge exchange and atomic polarizability and so registers a higher value (σ =2.0Å^3 at the CCSD(t) level). Polarizability perpendicular to the bond is only composed of atomic polarizabilities (σ =0.7Å^3). An EE based dynamic charge scheme can only reproduce polarization parallel to the bond, so polarizabilities perpendicular to the bond are zero. The solution we employ here for the COMB2011 potential is to place a point dipole on each atom similar to the fluctuation charge-fluctuating point dipole model by Sterne et al.[52]

With the fluctuating dipole model, the polarization vector is calculated directly from the electrostatic field generate by the atomic charges, $\vec{E}_i^q$, and the neighboring induced dipoles.

$$\vec{\mu}_i = P_i \vec{E}(\vec{r}) = P_i \left[\vec{E}_i^q + \sum_{j=1, j \neq i}^{N} T_{ij} \vec{\mu}_j \right] \quad , \tag{34}$$

$$\vec{E}_i^q = \frac{1}{4\pi\varepsilon_0} \sum_{j \neq i}^{N} q_j \frac{\partial J_{ij}^{qq}}{\partial r} \frac{\vec{r}_{ij}}{|\vec{r}_{ij}|} \quad , \tag{35}$$

where, P_i is the polarizability tensor and T_{ij} is the dipole-dipole interaction tensor. For atoms with isotropic polarizabilities, as is the case here, P reduces to a scalar value. Induced dipoles calculated in this manner suffer the same instability at close approach as the variable charges.[53] Consequently, T_{ij} is employed as a damped function that diminishes as atoms overlap. For consistency, the same damping that is used with the Coulombic interactions is applied here:

$$T_{ij} = \frac{1}{4\pi\varepsilon_0 \left|\vec{r}_{ij}\right|^3} \left(1 - 3\frac{\vec{r}_{ij} \cdot \vec{r}_{ij}}{\left|\vec{r}_{ij}\right|^2}\right)\left[1 - e^{-2\zeta_i r}\left(1 + 2\xi_j r_{ij} + 2\xi_j^2 r_{ij}^2\right)\right] \qquad . \tag{36}$$

The additional energy contributions are the dipole self energy, the dipole-charge interaction and the dipole-dipole interactions:

$$U[\{q\}; \{\mathbf{r}\}] = \sum_i V_i^{Self}(q) + \tfrac{1}{2}\sum_i \sum_{j\neq i} q_i J_{ij}^{qq} q_j + \sum_i \sum_{j\neq i} q_i J_{ij}^{qz} Z_j + \tfrac{1}{2}\sum_i \sum_{j\neq i} V_{ij}^{Bond}(r_{ij})$$
$$+ \sum_i \frac{\vec{\mu}_i^2}{2\alpha_i} + \sum_i \vec{\mu}_i \cdot \vec{E}_i^q + \tfrac{1}{2}\sum_i \sum_{j\neq i} \vec{\mu}_i T_{ij} \vec{\mu}_j \qquad . \tag{37}$$

Atomic polarizabilities are fit to reproduce the polarizability of the O_2 dimer as well as the dissociation curve of the O_2^- anion. The point dipole model affects the parameterization since a larger induced dipole moment exists when charge is localized on one atom rather than distributed equally between atoms. As the bond is stretched, charge localizes on one atom and the two atoms separate as atomic oxygen and an oxygen anion.

Figure 2 shows the CCSD(t) calculated and COMB2011 fit dissociation curve for several oxygen anions. It indicates that both the fit and calculated values predict O_2^{1-} to be the most stable form of molecular oxygen with an extended bond length. Atomic parameters for oxygen are presented in Table 1 and O-O interaction parameters are listed in Table 2A and B.

2.5.3 Parameterization of copper oxide

The energies for the oxide phases are fit to the enthalpy of formation, $\triangle H_f$, at 0K rather than the cohesive energy. This allows for a comparison between phases of different stoichiometry and charge states. $\triangle H_f$ is determined as the total energy of the oxide phase minus the energy of the reactants in their reference states: $O_{2(g)}$ and $Cu_{(s)}$. Calculations are performed on ideal structures at 0K for comparison to first principles calculations where appropriate. The copper-oxygen interaction parameters and charge dependent copper parameters are fit using a weighted least squares best fit to $\triangle H_f$ of the cuprite phase of Cu_2O, CuO in the monoclinic ground state and high pressure NaCl and CsCl phases, and the metastable paramelaconite phase of Cu_4O_3. The energy vs. isometric strain and the unrelaxed elastic constants for Cu_2O are also included in the fitting data set. Additionally, the training set includes the $\triangle H_f$ of a series of phases that are not manifested in the phase diagram; however, it is important to verify that the potential does not predict any of these to be more stable than the experimentally displayed phase. The additional structures examined have various coordination numbers on Cu: the anti-fluorite of Cu_2O (4 on Cu) and CuO_2 as fluorite (8 on Cu), α-cristobalite (4 on Cu) and β-cristobalite (4 on Cu).

As in the case of the metallic phase, formation enthalpies of the oxides are calculated using DFT with *VASP* 4.6. Energies are determined using the same functional, energy cutoff and k-point mesh as were used for the metallic phase. The equilibrium lattice parameters for the ground state are scaled to experimental values for cuprous and cupric oxide. Energy vs. isometric strain is determined relative to the scaled lattice constant. DFT typically underestimates the $\triangle H_f$ for copper oxides with reported values around -1.24 eV[54, 55] compared to experimental values of -1.75 eV[56]. This is mainly due to the over-binding of the O_2 reference state in DFT. In this work, the energy of the O_2 molecule is fit to a higher level of theory than DFT, which reproduces the

experimental bond enthalpy with greater accuracy. With the improved reference state energy for O_2, the fitted $\triangle H_f$ for Cu_2O of 1.78eV deviates from experimental values by only 1.6%.

The difficulties with the O_2 reference state in DFT also apply to defect formation enthalpies, $\triangle H_f^{def}$[57] Consequently, values for $\triangle H_f^{def}$ for point defects and surface energies that provide a reliable comparison to this potential are not available. $\triangle H_f^{def}$ for point and planar defects are thus used only for qualitative assessment of the final potential parameters. Finally, charge dependent parameters are fit with the additional constraint that the electronegativity on each atom is 1.0×10^{-6} eV/q in the ideal Cu_2O structure. This ensures the ground state is a minimum in both real space and charge space. The full list of interaction parameters are tabulated in Tables 2A, 2B and Table 3.

3. Results and Discussion

3.1 Properties of metallic copper

Properties of the metallic phase as predicted by the potential are compared in Table 4 to experiment, values calculated from first principles, results for Mishin's EAM potential , Yu's previous Cu potential[34, 58], and ReaxFF potential.[29] Elastic properties and surface energies are fit to values determined with fixed nuclear positions; however the values listed in Table 4 are determined with relaxed nuclear positions. The final parameter set reproduces the experimental elastic moduli and the C_{11} and C_{12} elastic constants. However, the C_{44} elastic constant is about 30% lower than the calculated values. This weakness of the potential was also present in the earlier COMB parameterization.[34] The cohesive energies of the HCP, BCC, simple cubic and diamond cubic phases are included in the training set. The values in Table 4 are based on optimized structures using the final parameter set. The simple cubic and diamond cubic phases

are fit with fairly low weight which is reflected in the larger deviations from calculated values. However, the correct qualitative trends are maintained for these low coordination phases.

The formation enthalpies for common point defects and the stacking faults in the (111) plane are calculated as a validation of the potential. The results are listed in Table 4 and compared to published reference values. The calculations for both planar and point defects are performed on a 36x36x36 $Å^3$ supercell with periodic boundary conditions applied in three dimensions; the point defects are optimized at constant volume. The planar defect structures are allowed to relax their volume in the direction normal to the plane of the defect using a steepest descent algorithm. The energies are determined with dynamic charge equilibration. The point defect formation energy is determined relative to the reference state, which is defined as the total energy per atom in the perfect FCC lattice according to the following equation:[59]

$$E_F = nE_{Def} - (n \pm 1)E_{Cu} \qquad . \tag{38}$$

Here, n is the number of atoms in the defect structure, E_{def} is the energy per atom in the defect structure, and E_{cu} is the energy per atom in the perfect FCC lattice. The predicted formation energies for Cu vacancies and the octahedral interstitial agree with experimental values[60] and other simulation methods. A calculation of the formation energies of the three dumbbell interstitials shows the 100 dumbbell to be the most energetically favorable interstitial, with a defect formation energy of 2.48 eV, in good agreement with experimental values.[60]

The relative energies for the (111), (100) and (110) surfaces agree with the values calculated from first principles[34] with a mean error of 3.8%. The surfaces take on a slight charge when relaxed with dynamic charge equilibration. The surface charge reflects the change in electron density due to the change in coordination at the surface. This is indicated in Figure 3 which shows planes parallel to the (100) surface. As indicated in the figure, the (100) surface

takes on a slight negative charge. The charge alternates between positive and negative with each

subsequent plane down from the surface and returns to charge neutrality within seven lattice

planes. The graph in Figure 3 shows the variation in planar average charge density as determined

by the potential. The charge returns to neutral about 10 Å from the surface. The values in

parentheses in Table 4 are determined with a charge of zero on each atom and no dynamic

charge equilibration. The results are equivalent, indicating that the surface charge does not

contribute significantly to the total surface energy for a pure metal.

Calculated formation enthalpies for the stacking faults reflect trends predicted by the

other reference methods. As shown in Table 4, the potential predicts a higher formation energy

for the intrinsic stacking fault than the COMB2010 parameterization. Examining the COMB2011

potential, the predicted formation energy is closer to experimental values, but differs from DFT

values[34] by a greater degree. The predicted extrinsic stacking fault energy is improved over the

COMB2010 potential; however, the unstable stacking fault energy is underestimated by

COMB2011 parameter set relative to all other referenced methods. The reason for the

underestimation of stacking fault energies is directly influenced by the Legendre polynomial

bond angle correction terms. A careful fine-tuning of the polynomial parameters in subsequent

versions of the potential can improve its performance in applications where improved

mechanical properties of the metal are required. Here, however, the angular corrections for the

metal are tuned to optimize properties of the metal and the oxide phases, rather than the metal

alone.

As with surfaces, the unstable stacking fault and point defect energies take on a slight

charge reflecting the change in coordination. The results of the calculations performed without

variable charges are listed in parentheses alongside the charge optimized values in Table 4. The

fact that the results are the same indicates that the effect of charge on pure metal planar defects is very slight. The differences between this parameterization of the COMB2011 potential and that of and Yu *et al.*[34] are, therefore, attributable to the refitting of the parameters rather than the inclusion of electrostatic interaction.

3.2 Properties of molecular oxygen

The self energy functions for both elements are determined as the least squares best fit to calculated values for electron affinities and ionization potentials. The success of the COMB2011 fit is reflected in the values listed in Table 5. COMB2011 potential is able to capture the dissociation behavior of oxygen and its anions as illustrated in Figure 2. COMB reproduces the lowest energy state of O_2 to be the O_2^- anion with a charge of -0.5 on each atom, which is consistent with higher level calculations that predict the lowest energy charge state to be O_2^-. The O_2^{2-} anion from COMB2011 is unstable until it dissociates into separate O^- anions. This agrees well with *ab initio* methods up to CCSD(t)/aug-cc-pVTZ level of theory.

The polarizability of oxygen is fit along with the other electrostatic parameters. The starting point for the fit is the atomic polarizability calculated to be 0.716 Å^3 using CCSD(t)/cc-pVTZ. The fitted value of 0.36 Å^3 underestimates the atomic values but successfully reproduces the components of the polarizability tensor of the O_2 molecule as shown in Table 6.

3.3 Properties of copper oxide

The lattice parameter, formation enthalpy, unrelaxed bulk modulus, shear modulus and the C_{11}, C_{12} and C_{44} elastic constants for Cu_2O are included in the training data set. The results in Table 7 are for relaxed atomic positions. The C_{44} elastic constant exhibits a large drop due to ionic relaxation and consequently exhibits a larger deviation from the reference values. The

25

COMB2011 parameterization shows significant improvement over the COMB2010

parameterization and reproduces the properties from first-principles calculations.

For the oxide phases, defect formation enthalpies $\triangle H_f^{def}$ must consider the chemical

potential of species added or removed from the system[54]:

$$\Delta H_F^{Def} = E_{Def} - E_0^{Bulk} \pm \sum_i n_i \mu_i \qquad . \tag{39}$$

Here, μ_i is the chemical potential of species i and n_i is the number of atoms of species i added or

removed from the perfect structure to form the defect. E_{Def} is the energy of the defect structure

and E_0^{Bulk} is the energy of the perfect structure. μ_i depends on the conditions under which the

defect is formed such that $\mu_i = \mu^* - \triangle\mu$, where μ^* is the chemical potential of the reference

state.[54] For Cu_2O to form, the relationship $2\mu_{Cu} + \mu_O = \mu_{Cu2O}$ must be true. Furthermore, if we

neglect the small dependence on pressure of μ_{Cu2O}, then $2\mu_{Cu} + \mu_O = \triangle H_{f\text{-}Cu2O}$. In the copper

rich (oxygen lean) limit, where Cu_2O is in equilibrium with metallic Cu, μ_{Cu} is equal to the

chemical potential of metallic Cu, $\mu_{Cu(s)}$, which in COMB is taken as the total energy per atom

in the perfect FCC lattice. On the contrary in the oxygen rich limit μ_{Cu} is zero and $\mu_O = \triangle H_{f\text{-}Cu2O}$.[54, 55, 61]

For comparison, values for $\triangle H_f^{def}$ are determined at the copper rich limit for several

point defects; the results are listed in Table 7. The relative energies for the oxygen defects, V_o

and O_i from COMB2011 agree qualitatively with the results of first principles calculations[54, 55, 61];

however a large discrepancy is shown for V_O described by COMB2010. In addition, the

formation enthalpies for V_{Cu} from both COMB potentials are higher than the experimental

reference values. However, here and in the DFT reference values, the $\triangle H_f^{def}$ is determined for

the charge neutral defect, meaning V_{Cu} is formed by removing a neutral Cu atom from the ideal crystal. This is unlikely in real systems where an ion is more likely to be removed. A lower energy charged defect most likely accounts for the discrepancy between the experimental and computational results. $\triangle H_f^{def}$ for Cu interstitials from COMB2010 are slightly negative, which is mainly due to the strong covalent attraction between cations. $\triangle H_f^{def}$ for other defects agree qualitatively with the DFT values considering that μ_O varies by 0.51 eV between DFT and COMB.[55]

In a manner similar to point defect calculations, the surface energies of the oxide consider the chemical potential of the species added or removed from the perfect crystal to form the surface.[55]

$$\gamma = \frac{1}{A}\left(G \pm \sum_i n_i \mu_i\right) \ . \tag{40}$$

Here, A is the surface area and γ is the surface free energy. In the COMB potential, the calculations are performed at 0K, where contributions due to entropy are zero, allowing direct comparison with reported DFT values. μ_{Cu} and μ_O at the oxygen lean limit are used for comparison to reported values under similar conditions.[55] The (111) surface is the only stoichiometric surface listed in Table 7. This surface also gives the best agreement between methods. A general trend of the surface energies is exactly reproduced: oxygen terminated surfaces have lower surface energies than copper terminated ones. It is also found the CuO terminated (110) surface is the most stable surface of Cu_2O.

Since Cu_2O is not the only possible oxide form of Cu, the properties of monoclinic CuO are also considered in the fitting scheme. The modeling of CuO is complicated by the symmetry breaking Jahn-Teller distortion that characterizes structures containing d^9 transition metals.[62] The

effect cannot be modeled with current DFT implementations.[57] Classical potentials have had better success in replicating the effect where, the Cu^{2+} cation is modeled as an aspherical ion with a distorted neighbor shell.[62] This special feature of Cu^{2+} cation has also been shown to pose an effect to the Jahn-Teller distortion of $[Cu(OH_2)_6]^{2+}$ molecules.[29] The COMB formalism has two means of replicating asymmetry in the neighbor shell: the Legendre polynomial angle correction and the point dipole model. In this work, only the CuO heat of formation, rather than the structural properties (particularly the lattice parameters) is fit explicitly; however the lattice parameters were utilized to check if the parameter set reasonably predicts the CuO structure. It is presented in Table 8 that COMB2011 potential predicts the properties of this phase with reasonably well fidelity. Although the lattice parameters deviate from the low temperature values[34], the total volume of the structure is comparable to DFT results as shown in Figure 4. Polarization does not improve the results, as shown the last column in Table 8.

Table 9 lists $\triangle H_f$ for several oxide phases from experimental, first-principles calculations, ReaxFF potential and COMB2011 potential. The experimental $\triangle H_f$ for Cu_4O_3 is lower in energy than Cu_2O indicating that Cu_2O is only stable under oxygen lean conditions.[63] As shown in Table 9, the relative formation enthalpies for the three low energy oxide phases as predicted by the COMB2011 potential are consistent with experimental values. This is further illustrated in Figure 4, which plots the energy per unit volume for the three low energy phases. In Figure 4 the volume and energy vs. isometric strain for the CuO and Cu_2O structures compare well with values from DFT.

It should be noted that the ReaxFF potential for $Cu/Cu_2O/H_2O^{29}$ yields very reasonable properties, which are very comparable to that from COMB2011, for both Cu and Cu_2O considered, as presented in Tables 4 and 9. This is not surprising since there are significant

overlaps between the training databases of the ReaxFF and COMB potentials. It should be
expected that this ReaxFF potential produces reliable properties for the Cu/Cu$_2$O interfaces, as
well as Cu oxidation processes. A comparison of the Cu surface oxidation process and oxide
growth with both ReaxFF and COMB potentials is reserved for future studies.

3.4 Behavior of O$_2$ on the Cu surface

3.4.1 Molecular Oxygen adsorption on Cu (100) surface

The behavior of O$_2$ on the Cu (100) surface as predicted by COMB2011 is used as a test
of the potential. The enthalpy of adsorption, $\triangle H_{Ads}$, and dissociative adsorption of O$_2$ on the
Cu(100) surface is determined by placing O$_2$ at several sites and minimizing the energy of the
structure via a steepest descent algorithm. $\triangle H_{Ads}$ is determined using an equation similar to
Equation 41:

$$\Delta H^{Ads} = E_{Cu-O_2}^{(100)} - E_{Cu(s)}^{(100)} - \mu_{O_2} \qquad .\tag{41}$$

$E_{Cu(s)}^{(100)}$ is the energy of the Cu substrate with a free (100) surface. $\triangle H_{Ads}$ is determined under
oxygen rich conditions, where μ_O=1/2 E$_{O2(g)}$.[54]

The images to the left in Figures 5 (a) – (f) show the initial sites selected for study. The
results are compared with values calculated via DFT in Table 10. When the initial position of the
O$_2$ molecule is 2 Å above the metal surface, the molecule relaxes to a local minimum that is 2.18
Å above the surface with a $\triangle H_{Ads}$ of -2.51 eV. The molecule does not dissociate at this point and
only a small charge of -0.092 is transferred to the molecule. When the O$_2$ is placed 1.8 Å above
the surface, the molecules relax toward the surface and dissociates at top sites but not at bridge
and hollow sites. The relaxed positions are shown to the left of Figures 5 (a) – (f). The energies
in Table 10 indicate that the lowest $\triangle H_{Ads}$ occurs when an O$_2$ molecule is positioned at a top site

and relaxes to a state where the O atoms are dissociated and absorbed into neighboring 4-fold hollow sites. This corresponds to the configuration shown in Figure 5 (c), and the label Top 1 in Table 10. The third row in Table 10 lists the final height of the oxygens on the Cu surface, and Top 1 site also exhibits the lowest height since O atoms are adsorbed on to the hollow sites. We have also investigated the values of $\triangle H_{Ads}$ determined with the point dipole contribution turned off, whereas the overall effect is only ~0.1 eV. COMB values for $\triangle H_{Ads}$ are compared to values determined via first principles calculations. In particular COMB and DFT give the same relative trends, both predicting dissociation to the hollow sites as being most energetically favorable.

The last row in Table 10 lists the energy barrier, $\triangle H_{Bar}$, for O_2 to dissociate on each site calculated from COMB; it is shown that O_2 dissociation reactions on these sites are endothermic. The energy barriers for the top sites, ~0.1 eV, are the lowest compared to other sites; consistent with the dissociation behaviors. Additionally, the dissociation energy barrier for the Hollow 2 site from the COMB predicted energy barrier value is 0.3 eV; although 2.3 times larger than our first-principles DFT calculations (0.13 eV), considering this is a pure prediction, instead of a fitted property, COMB2011 potential is reasonably predicting the dissociation of O_2 on Cu (100) surface.

3.4.2 Oxidation of Cu(100) surfaces

The copper oxide is the promising nanostructure for microelectronic devices because of its diverse morphologies of Cu_2O island with difference temperatures. Therefore, oxygen coverage on Cu (100) surface and the resulted reconstructions have been the subject of numerous theoretical and experimental studies.[64-73] With STM technique, different reconstructed Cu (100) surfaces which depend on the oxygen coverage are observed.[72, 73] At oxygen coverage less than 0.3 monolayers (ML), the surface is characterized by micro-domains formed in a c(2x2)

arrangement, which can be describe as oxygen atoms occupying the 4-fold hollow sites. When the oxygen coverage rises above 0.5 ML, the missing-row $2\sqrt{2} \times \sqrt{2}\ R45^0$ reconstructed surface will be induced.[72, 73] To study the interaction between oxygen molecules and the Cu surfaces with MD simulations, oxygen molecules are placed on Cu (100) surface, roughly 3Å ~ 5Å. The oxygen partial pressure is estimated around 100 oxygen atoms. The surface structure is composed of clean Cu (100) without oxygen at the sub-surface and missing-row reconstructed surface. Further, this structure was then annealed for 10ps at 1000 K. Figure 6(a) illustrates the interaction between oxygen molecules and the clean Cu (100) surface. It indicates that 30% of the oxygen molecules are adsorbed with positively charged oxygen atom pointing toward the hollow sites of the Cu surface. The first dissociation of oxygen molecule on the clean Cu (100) surface was observed at the frame of 2 ps, and second one was observed sequentially at the frame of 2.7 ps. Figure 6(b) indicates that the dissociated oxygen atoms with negative charge are located stably at the hollow site of Cu (100) surface.

In contrast to the clean Cu (100) surface, dissociated oxygen atoms have not been observed on the top of missing-row reconstructured surface for 10 ps. It has been reported that oxygen-induced reconstructed Cu (100) surface shows repulsive characteristics to oxygen molecules,[74] which implies that the sub-surface oxygen atoms may induce a strong barrier for further dissociation of oxygen molecules. Therefore, higher surface temperatures or long-time scaled methods are needed for this investigation. In summary, COMB2011 potential demonstrates that oxygen is molecularly adsorbed on the clean Cu (100) surface and migrates until sites with lower dissociation barrier are found. The potential indicates that the dissociations are taking place when the oxygen molecules are moving close on the hollow site of Cu (100) surface. To further investigate the transition from missing-row reconstructed surface to Cu_2O

islands, which involves longer-time scaled simulations, we are currently implementing the COMB potentials within the adaptive kinetic Monte Carlo (AKMC).[75]

3.5 Simulations of the $Cu_2O(111)\|Cu(100)$ interface

The metal-oxide interface is not well characterized in the literature. This is partly due to the graded nature of the most interfaces, which form from an oxygen-induced reconstructed surface. One means of obtaining an atomically sharp interface is through the electrochemical deposition of Cu_2O.[76] When deposited on the Cu (100) surface, Cu_2O forms a film with initial growth in the (111) direction.[76] The resulting $Cu_2O(111)\|Cu(100)$ interface is atomically sharp and suspected to be semi-coherent, although this exact structure has not been confirmed experimentally. As a final check of the potential, a model of the interface is relaxed and annealed at 50, 100, 200, 300 and 450 K using the COMB2011 potential. The model consists of a $35.3x31.4x36.2$ Å^3 supercell containing a 20 Å thick slab of $Cu_{(s)}$ interfaced with a 15.3 Å thick slab of Cu_2O. Periodic boundary conditions are applied in three dimensions; in other words, no vacuum space exists between the slabs, so the periodic image is one of alternating metal and oxide slabs stacked upon one another.

The epitaxial relationship between the metal and oxide is $Cu_2O(111)[11\overline{2}]\|Cu(100)[001]$, which gives a lattice mismatch of 3.64% along the epitaxial direction. The slab is annealed under constant temperature and pressure (NPT) for 10 ps at each temperature. An MD timestep 0.1 fs is used. The temperature is maintained via a Nosé-Hoover thermostat.[77-79] The system cell is fixed in three dimensions; during relaxation, the symmetry of the supercell is constrained to remain orthorhombic. After relaxation the adhesion energy of the interface is estimated to be 2.77 J/m^2, compared to 1.58 J/m^2 from our first-principles calculations.

The interface is predicted to be stable at all the temperatures considered. The first interfacial layers in both phases rearrange beginning at 100 K suggesting either a lower energy epitaxial relationship or reconstruction exist. Figure 7 shows the interface after annealing for 10 ps at 300 K, viewed along the Cu [100] or $Cu_2O[11\overline{2}]$ direction. During the simulation there is no evidence of a phase transformation beyond the first layer or atomic diffusion between phases suggesting the potential is predicting the correct ground state configuration. There is also only a negligible charge transfer between phases, as indicated in Figure 8, which shows the planar average charge density with distance from the interface. The figure indicates that charge transfer is limited to the interfacial region of one Cu layer in the oxide and 1-2 layers in the metal. The charge leaking across the Cu/Cu_2O interface is negligible, which is a result of the field effect (Eq. 33). However in the original charge model employed by the first-generation COMB potential for SiO_2[24], the charge leaking across the Si/SiO_2 interface is significant, which leads to unphysical negatively charged first layer Si atoms in the Si substrate (Fig. 9 of Ref. [24]). This deficiency is rectified with the improved charge model presented in this work.

Considering the computational efficiency of the COMB2011 potential presented in this work, the charge equilibration step is the most time-consuming part in the calculations. A benchmark test of the COMB potential implemented in the Large-scale Atomic/Molecular Massively Parallel Simulator[80] (LAMMPS) software showed that when compared to the Lennard-Jones potential, COMB potential take approximately ~280 factors more computational time. Compared to Tersoff[22], AIREBO[81] and ReaxFF[40] potentials implemented in the same software, COMB potential take approximately 70, 5 and 1.5 factors more time.

4. Conclusions

Based on results from the simulations and calculations, a reactive potential composed of a short-range bond order potential coupled with variable charge electrostatics is shown to be capable of simulating the ground state bonding environments of Cu as both a pure metal and when oxidized to Cu_2O. The potential also captures the bonding behavior of oxygen as a pure element interacting with $Cu_{(s)}$ and when incorporated in the Cu_2O oxide. This enables the large scale simulation of processes such as oxidation of the metal surface or phenomena across the metal oxide interface.

The potential successfully produce a monoclinic unit cell for the higher oxide CuO with the correct volume and formation enthalpy but noticeable deviated lattice parameters. Since the relative energy for the phases are consistent with experimental values, the potential is useful for studies of the initial stages of oxidation up until the formation of CuO. Future work should seek to improve the potential in this regard. Lastly, the simulations performed in the course of this work are only intended to demonstrate the stability and capabilities of the potential formalism. The statistics are not sufficient to draw any quantitative conclusions about the materials themselves. Instead, a more thorough examination of the materials and processes simulated here are left for future work.

Acknowledgements:

References

[1] L. O. Brockway, and I. M. Adler, J. Electrochem. Soc. **119**, 899 (1972).

[2] K. Heinemann, D. B. Rao, and D. L. Douglass, Oxidation of Metals **9**, 379 (1975).

[3] R. H. Milne, and A. Howie, Philosophical Magazine a-Physics of Condensed Matter Structure Defects and Mechanical Properties **49**, 665 (1984).

[4] A. Ronnquist, and H. Fischmeister, J. Instit. Metals **89**, 65 (1960).

[5] F. W. Young, J. V. Cathcart, and A. T. Gwathmey, Acta Metallurgica **4**, 145 (1956).

[6] G. A. Kaminski, H. A. Stern, B. J. Berne, R. A. Friesner, Y. X. X. Cao, R. B. Murphy, R. H. Zhou, and T. A. Halgren, J. Comput. Chem. **23**, 1515 (2002).

[7] J. C. Yang, M. Yeadon, B. Kolasa, and J. M. Gibson, Microsc. Microanal. **4**, 334 (1998).

[8] N. Cabrera, and N. F. Mott, Reports on Progress in Physics **12**, 163 (1948).

[9] K. Tanaka, T. Inomata, and M. Kogoma, Thin Solid Films **386**, 217 (2001).

[10] J. C. Yang, D. Evan, and L. Tropia, Appl. Phys. Lett. **81**, 241 (2002).

[11] J. C. Yang, B. Kolasa, J. M. Gibson, and M. Yeadon, Appl. Phys. Lett. **73**, 2841 (1998).

[12] L. Sun, and J. C. Yang, J. Mater. Res. **20**, 1910 (2005).

[13] R. H. Milne, Surf. Sci. **232**, 17 (1990).

[14] R. Drautz, D. A. Murdick, D. Nguyen-Manh, X. W. Zhou, H. N. G. Wadley, and D. G. Pettifor, Phys. Rev. B **72**, 144105 (2005).

[15] D. G. Pettifor, M. W. Finnis, D. Nguyen-Manh, D. A. Murdick, X. W. Zhou, and H. N. G. Wadley, Mater. Sci. Eng., A **365**, 2 (2004).

[16] R. W. G. Wyckoff, *Crystal Structures* (Interscience Publishers, New York, 1963).

[17] N. E. Brese, M. Okeeffe, B. L. Ramakrishna, and R. B. Vondreele, J. Solid State Chem. **89**, 184 (1990).

[18] M. S. Daw, and M. I. Baskes, Phys. Rev. B **29**, 6443 (1984).

[19] M. W. Finnis, and J. E. Sinclair, Philosophical Magazine a-Physics of Condensed Matter Structure Defects and Mechanical Properties **50**, 45 (1984).

[20] F. H. Streitz, and J. W. Mintmire, Phys. Rev. B **50**, 11996 (1994).

[21] J. Tersoff, Phys. Rev. B **37**, 6991 (1988).

[22] J. Tersoff, Phys. Rev. B **38**, 9902 (1988).

[23] A. Yasukawa, JSME INT J A-MECH M **39**, 313 (1996).

[24] J. G. Yu, S. B. Sinnott, and S. R. Phillpot, Phys. Rev. B **75**, 085311 (2007).

[25] T.-R. Shan, B. D. Devine, J. W. Hawkins, A. Asthagiri, S. R. Phillpot, and S. B. Sinnott, Phys. Rev. B **82**, 235302 (2010).

26   K. Chenoweth, A. C. T. van Duin, P. Persson, M. J. Cheng, J. Oxgaard, and W. A. Goddard, J. Phys. Chem. C **112**, 14645 (2008).

27   D. Raymand, A. C. T. van Duin, M. Baudin, and K. Hermansson, Surf. Sci. **602**, 1020 (2008).

28   Q. Zhang, T. Cagin, A. van Duin, W. A. Goddard, Y. Qi, and L. G. Hector, Phys. Rev. B **69** (2004).

29   A. C. T. van Duin, V. S. Bryantsev, M. S. Diallo, W. A. Goddard, O. Rahaman, D. J. Doren, D. Raymand, and K. Hermansson, J. Phys. Chem. A **114**, 9507 (2010).

30   D. W. Brenner, Physica Status Solidi B-Basic Research **217**, 23 (2000).

31   T. Iwasaki, and H. Miura, J. Mater. Res. **16**, 1789 (2001).

32   T. Iwasaki, J. Mater. Res. **19**, 1197 (2004).

33   T. Iwasaki, J. Mater. Res. **20**, 1300 (2005).

34   J. Yu, S. B. Sinnott, and S. R. Phillpot, Philos. Mag. Lett. **89**, 136 (2009).

35   R. G. Parr, R. A. Donnelly, M. Levy, and W. E. Palke, J CHEM PHYS **68**, 3801 (1978).

36   T.-R. Shan, University of Florida, 2011.

37   A. K. Rappe, and W. A. Goddard, J. Phys. Chem. **95**, 3358 (1991).

38   D. Wolf, P. Keblinski, S. R. Phillpot, and J. Eggebrecht, J. Chem. Phys. **110**, 8254 (1999).

39   T.-R. Shan, B. D. Devine, T. W. Kemper, S. B. Sinnott, and S. R. Phillpot, Phys. Rev. B **81**, 125328 (2010).

40   A. C. T. van Duin, S. Dasgupta, F. Lorant, and W. A. Goddard, J. Phys. Chem. A **105**, 9396 (2001).

41   G. D. Purvis, and R. J. Bartlett, J. Chem. Phys. **76**, 1910 (1982).

42   T. H. Dunning, J. Chem. Phys. **90**, 1007 (1989).

43   M. J. Frisch, H. B. Schlegel, and G. E. Scuseria, (Gaussian Inc., Wallingford CT., 2004).

44   E. Ruiz, S. Alvarez, P. Alemany, and R. A. Evarestov, Phys. Rev. B **56**, 7189 (1997).

45   K. Takahashi, A. Itoh, T. Nakamura, and K. Tachibana, Thin Solid Films **374**, 303 (2000).

46   G. Kresse, and J. Hafner, Phys. Rev. B **47**, 558 (1993).

47   P. E. Blochl, Phys. Rev. B **50**, 17953 (1994).

48   J. H. Rose, J. R. Smith, F. Guinea, and J. Ferrante, Phys. Rev. B **29**, 2963 (1984).

49   P. Geerlings, F. De Proft, and W. Langenaeker, Chemical Reviews **103**, 1793 (2003).

50   H. Toufar, K. Nulens, G. O. A. Janssens, W. J. Mortier, R. A. Schoonheydt, F. DeProft, and P. Geerlings, J. Phys. Chem. **100**, 15383 (1996).

51   B. G. Dick, and A. W. Overhauser, Phys. Rev. **112**, 90 (1958).

52   H. A. Stern, G. A. Kaminski, J. L. Banks, R. H. Zhou, B. J. Berne, and R. A. Friesner, J. Phys. Chem. B **103**, 4730 (1999).

53   B. T. Thole, Chem. Phys. **59**, 341 (1981).

54   H. Raebiger, S. Lany, and A. Zunger, Phys. Rev. B **76**, 045209 (2007).

55   A. Soon, X. Y. Cui, B. Delley, S. H. Wei, and C. Stampfl, Phys. Rev. B **79**, 035205 (2009).

56   D. R. Lide, *CRC Handbook of Chemistry and Physics* (CRC Press, Boca Raton, FL, 2005).

57   D. O. Scanlon, B. J. Morgan, and G. W. Watson, J. Chem. Phys. **131** (2009).

58   Y. Mishin, D. Farkas, M. J. Mehl, and D. A. Papaconstantopoulos, Phys. Rev. B **59**, 3393 (1999).

59   Finnis. M, *Interatomic Forces in Condensed Matter* (Oxford University Press, Oxford, 2003).

60   M. Sprik, J. Phys. Chem. **95**, 2283 (1991).

61   M. Nolan, Thin Solid Films **516**, 8130 (2008).

62   S. M. Woodley, P. D. Battle, C. R. A. Catlow, and J. D. Gale, J. Phys. Chem. B **105**, 6824 (2001).

63   K. J. Blobaum, D. Van Heerden, A. J. Wagner, D. H. Fairbrother, and T. P. Weihs, J. Mater. Res. **18**, 1535 (2003).

64   M. J. Harrison, D. P. Woodruff, J. Robinson, D. Sander, W. Pan, and J. Kirschner, Phys. Rev. B **74**, 165402 (2006).

65   H. Iddir, D. D. Fong, P. Zapol, P. H. Fuoss, L. A. Curtiss, G. W. Zhou, and J. A. Eastman, Phys. Rev. B **76**, 241404 (2007).

66   K. W. Jacobsen, and J. K. Norskov, Phys. Rev. Lett. **65**, 1788 (1990).

67   F. Jensen, F. Besenbacher, E. Laegsgaard, and I. Stensgaard, Phys. Rev. B **42**, 9206 (1990).

68   T. Kangas, K. Laasonen, A. Puisto, H. Pitkanen, and M. Alatalo, Surf. Sci. **584**, 62 (2005).

69   I. Merrick, J. E. Inglesfield, and H. Ishida, Surf. Sci. **551**, 158 (2004).

70   I. K. Robinson, E. Vlieg, and S. Ferrer, Phys. Rev. B **42**, 6954 (1990).

71   S. Stolbov, A. Kara, and T. S. Rahman, Phys. Rev. B **66**, 245405 (2002).

72   K. Lahtonen, M. Lampimaki, M. Hirsimaki, and M. Valden, J. Chem. Phys. **129**, 194707 (2008).

73   K. Lahtonen, M. Hirsimaki, M. Lampimaki, and M. Valden, J. Chem. Phys. **129**, 124703 (2008).

74   M. Alatalo, A. Puisto, H. Pitkänen, A. S. Foster, and K. Laasinen, Surf. Sci. **600**, 1574 (2006).

75   G. Henkelman, and H. Jónsson, J. Chem. Phys. **111**, 7010 (1999).

[76] J. K. Barton, A. A. Vertegel, E. W. Bohannan, and J. A. Switzer, Chem. Mater. **13**, 952 (2001).

[77] W. G. Hoover, Phys. Rev. A **31**, 1695 (1985).

[78] S. Nose, J. Chem. Phys. **81**, 511 (1984).

[79] S. Nose, Mol. Phys. **52**, 255 (1984).

[80] S. J. Plimpton, Journal of Computational Physics **117**, 1 (1995).

[81] S. J. Stuart, A. B. Tutein, and J. A. Harrison, J. Chem. Phys. **112**, 6472 (2000).

[82] S. A. Adelman, and J. D. Doll, J. Chem. Phys. **64**, 2375 (1976).

[83] G. simons, and H. wang, *Single Crystal Elastic Constants and Calculated Aggregate Properties* (MIT Press, Cambridge, 1977).

[84] R. W. Balluffi, and A. P. Sutton, Intergranular and Interphase Boundaries in Materials, Pt 1 **207**, 1 (1996).

[85] Y. Mishin, M. J. Mehl, D. A. Papaconstantopoulos, A. F. Voter, and J. D. Kress, Phys. Rev. B **63**, 224106 (2001).

[86] M. B. J. Wijesundara, Y. Ji, B. Ni, S. B. Sinnott, and L. Hanley, J. Appl. Phys. **88**, 5004 (2000).

[87] M. M. Beg, and S. M. Shapiro, Phys. Rev. B **13**, 1728 (1976).

[88] J. Hallberg, and R. C. Hanson, Physica Status Solidi **42**, 305 (1970).

[89] W. Pauli, Zeitschrift Fur Physik **31**, 765 (1925).

[90] A. Soon, M. Todorova, B. Delley, and C. Stampfl, Phys. Rev. B **75**, 125420 (2007).

Tables

Table 1. Atomic and electrostatic potential parameters

	COMB2010		COMB2011	
	Cu	O	Cu	O
X (eV·q^{-1})	0	5.634414	3.768251	4.700782
J (eV·q^{-2})	4.321185	6.064346	2.966470	5.064537
K (eV·q^{-3})	0	4.514270	0.515044	2.756183
L (eV·q^{-4})	0	1.330079	0.257522	0.992188
ξ (Å^{-1})	0.454784	2.243072	1.476344	3.012029
Z (q)	0	0	0.293153	0.030819
P (Å^3)	0	0	0.335000	0.323757
P^J_1 (eV·q^{-3}·r^{-3})	-0.274649	-0.971086	-0.470698	-0.054039
P^J_2 (eV·q^{-4}·r^{-5})	0.725710	-3.922011	1.086271	1.136518
D_u (Å)	-0.161007	-0.001120	-0.307561	-1.628749
D_l (Å)	0.167765	0.001480	0	0.244020
Q_u (q)	2	5.504600	2	6
Q_l (q)	-6	-1.834900	-6	-2
CN^*	0	0	2.2	4.2
γ_{Coord}	0	0	0.250000	0.249569
E_{Coord} (eV)	0	0	0.597603	1.934556

Table 2A. Bond dependent potential parameters for COMB2010

	Cu-Cu	O-O	Cu-O	O-Cu
A (eV)	952.6931	3326.690	2966.036	2966.036
B (eV)	146.9871	260.8930	19.58262	19.58262
$\lambda(\text{Å}^{-1})$	2.794608	5.360000	4.475962	4.475962
$\alpha(\text{Å}^{-1})$	1.681711	2.680000	1.275175	1.275175
β	0.140835	2	0.140835	2
η	1	1	1	1
m	1	1	1	1
c (rad.)	0	6.6	0	6.6
d (rad.)	1	1	1	1
h (rad.)	1	-0.229000	1	-0.229000
n_B	10	10	10	10
R_s (Å)	3.15	2.6	2.45	2.45
S_s (Å)	3.35	3.0	2.65	2.65

Table 2B. Bond dependent potential parameters for COMB2011

	Cu-Cu	O-O	Cu-O	O-Cu
A (eV)	712.3527	3523.359	598.29837	598.29837
B (eV)	102.8261	204.6259	102.5144	102.5144
$\lambda(\text{Å}^{-1})$	2.712035	5.516839	3.129308	3.129308
$\alpha(\text{Å}^{-1})$	1.467089	2.527568	1.433963	1.433963
β	0.231055	2	0.231055	2
η	1	1	1	1
m	1	1	1	1
c (rad.)	0	43.56000	1.739680	2.043622
d (rad.)	1	1	1	1
h (rad.)	1	-0.22000	-0.297973	0.449820
n_B	10	10	10	10
R_s (Å)	3.2	2.2	3.2	3.2
S_s (Å)	3.6	2.8	3.6	3.6

Table 3. Coefficients for charge independent bond angle energy functions

	Cu-Cu	O-O	Cu-O-Cu	O-Cu-O
K_{LP}^1 (eV)	0.073078	0.000000	0.069535	0.635646
K_{LP}^2 (eV)	0.000000	0.000000	0.000000	0.635646
K_{LP}^3 (eV)	0.019678	0.000000	0.100428	0.000000

Table 4. Properties of metallic copper

	Exp.	DFT [g]	EAM [f]	ReaxFF [h]	COMB2010	COMB2011
a (Å)	3.62[a]	3.64	3.62	3.7	3.62	3.62
Eo (eV/atom)	-3.54[b]	-3.50	-3.54	-3.49	-3.54	-3.54
Bulk Mod. (GPa)	139[c]	140	140		139	139
C_{11} (GPa)	170[c]	173	173		170	171
C_{12} (GPa)	123[c]	123	123		123	123
C_{44} (GPa)	75.8[c]	80.1	76.2		49	47.7
α ($10^{-6}K^{-1}$)	16.5[b]				14.5	16.9
ΔE_o Phase Transitions (eV/atom)						
HCP		0.006	0.008		0.008	0.008
BCC		0.038	0.046	0.065	0.017	0.014
Cubic		0.47	0.43	0.598	0.49	0.38
Diamond		1.04	1.08	0.882	0.94	0.99
ΔH_f Point Defects (eV)						
V_{Cu}	1.28[d]		1.27		1.21	1.17
$Cu_{i\text{-}oct}$	2.8-4.2[e]		3.06		2.41	4.93
*Cu$_i$ 100 dumbell	2.8-4.2					2.48
*Cu$_i$ 110 dumbell	2.8-4.2					6.91
*Cu$_i$ 111 dumbell	2.8-4.2					8.58
Planar Defects (mJ·m^{-2})						
$\gamma_{(100)}$	1780[f]	1478	1345		1599	1478 (1478)**
$\gamma_{(110)}$	1780	1609	1475		1646	1519 (1519)
$\gamma_{(111)}$	1780	1294	1239		1295	1218 (1218)
γ_{ISF}	61[g]	34.3	36.2		44.4	46.3 (46.3)
γ_{USF}	162	210	161		224	105 (105)
γ_{Twin}	24[g]	19.2	18.2		45	23.2 (23.2)

* Indicates predicted values. All other value are included in the training set

** Values in parentheses are determined with charge equilibration

[a] Reference [56]

[b] Reference [82]

[c] Reference [83]

[d] Reference [84]

[e] Reference [60]

[f] Reference [85]

[g] Reference [86]

[h] Reference [29]

Table 5. Ionization potentials (IP) and electron affinities (EA) in eV for Cu and O

Cu	Ab Initio	COMB2010	COMB2011
1st EA	1.08	4.32	1.08
1st IP	7.43	4.32	7.43
2nd IP	20.3	17.28	18.6
O			
1st EA	1.40	2.75	1.40
2nd EA	-6.08	1.84	-6.08
1st IP	13.5	17.54	13.5

Table 6. Properties of molecular oxygen

	Ab Initio	COMB2010	COMB2011
Bond Length (Å)	1.21*	1.20	1.21
Bond Energy (eV)	-5.17*	-5.11	-5.17
Polarizability of O_2 (Å^3)**			
α^{11}	2.0	--	2.2
α^{22}	0.69	--	0.65
α^{33}	0.69	--	0.65

* Reference [56]

* ccsd(t)/cc-pvTZ

Table 7. Properties of Cu$_2$O (cuprous oxide)

	Experiment	First Principles	ReaxFF [h]	COMB2010	COMB2011
a (Å)	4.27[a]	4.31[e]	4.24	4.25	4.27
E_{coh} (eV/Cu$_2$O)	11.3[b]	11.4[e]		11.9	11.4
ΔH_F (eV)	-1.73[b]	-1.24[e]	-1.96	-2.33	-1.75
Bulk Mod. (GPa)	112[c]	112		94	111
Shear Mod.(GPa)		8.15		46	8.27
C_{11} (GPa)	123[c]	123		105	122
C_{12} (GPa)	108[c]	107		89	105
C_{44} (GPa)	12[c]	12.1		71	57.3
Cu Charge				0.79	0.54
Point Defects in Cu$_2$O (eV)[g]					
V_{Cu}	0.45[d]	0.28-1.17[e]		1.34	2.49
V_{Cu_split}	0.25[d]	0.78 -1.24[e]			2.20
V_O		1.55[e]		5.68	0.95
O_{i_tet}		1.36-1.47[e]		1.74	0.71
O_{i_Oct}		1.69-1.9[e]		2.95	2.26
Cu_{i_tet}		1.47[e]		-0.18	0.95
Cu_{i_Oct}		1.9[e]		-0.17	0.97
Surface Energies (mJ·m^{-2})[g]					
Cu$_2$O(100):Cu		1570[f]		3483	1510
Cu$_2$O(100):O		1070[f]		1490	1030
Cu$_2$O(110):Cu		1790[f]		2428	2380
Cu$_2$O(110):CuO		417[f]		951	603
Cu$_2$O(111)		785[f]		1425	783

[a] Reference [16]

[b] Reference [56]

[c] Reference [87, 88]

[d] Reference [89]

[e] Reference [54, 55, 61]

[f] Reference [90]

[g] Defect formation and surface energies correspond to oxygen lean conditions.

[h] Reference [29]

Table 8. Properties of monoclinic CuO

	Experimental	COMB	COMB+Polar
a (Å)	4.68[a]	4.36	4.33
b (Å)	3.42[a]	3.74	3.77
c (Å)	5.13[a]	5.04	5.05
β (Deg.)	99.6[a]	97.1	97.1
ΔH_F (eV)	-1.63[b]	-1.68	-1.68

[a] Reference [17]
[b] Reference [56]

Table 9. ΔH_f (in eV) of copper oxides

	Structure	Experimental	DFT/Simulation	ReaxFF [e]	COMB
Cu_2O	Cuprite	-1.73^a	-1.24^b	-1.96	-1.75
CuO	Tenorite	-1.63^c	-1.11^b	-1.91	-1.63
Cu_4O_3	Paramelaconite	-4.72^c	-5.74^c		-5.11
CuO	CsCl		-0.53^d		-0.31
CuO	NaCl		-1.24^d	-1.05	-1.22
CuO_2	α-Cristobalite		-0.30^d		-1.58
CuO_2	β-Cristobalite		-0.34^d		-1.31
CuO_2	Fluorite		-1.29^d		-0.49
Cu_2O	Anti-Fluorite		-1.14^d		-0.44

[a] Reference [56]
[b] Reference [54]
[c] Reference [63]
[d] This work
[e] Reference [29]

Table 10. ΔH_{Ads} (in eV) and height (in Å) of O_2 on Cu(100) surface

	Hollow 1	Bridge 1	Top 1	Hollow 2	Bridge 2	Top 2
ΔH_{Ads} (DFT)	-2.0	-2.2	-2.2	-2.9	-4.0	-2.4
ΔH_{Ads} (COMB)	-0.1	-1.4	-3.4	-0.9	-0.1	-1.4
Height (COMB)	2.3	1.9	0.7	1.4	2.2	1.4
ΔH_{Bar} (COMB)	0.7	1.0	0.1	0.3	5.0	0.1

Figures

A) B)
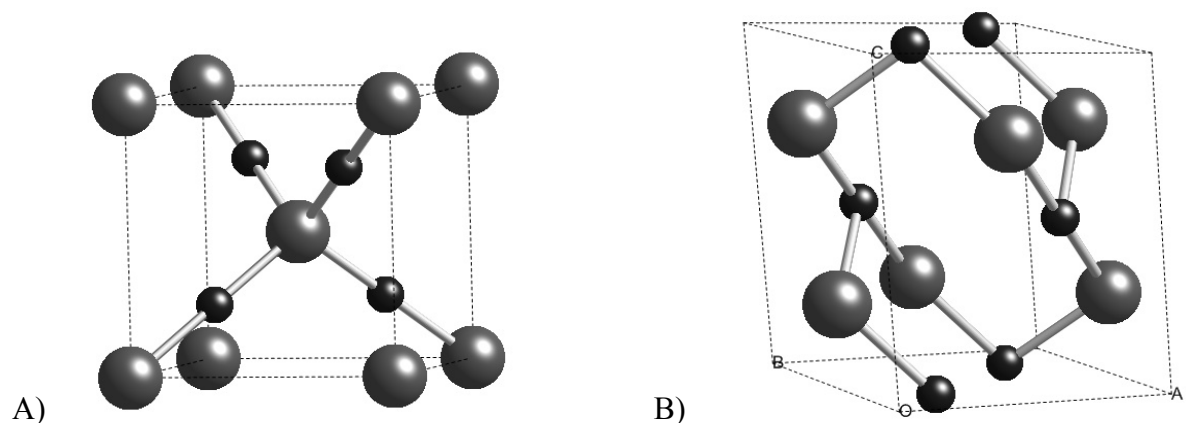
Figure 1. Crystal structures for the two low energy oxide phases of copper oxide. Large grey spheres represent O and small black spheres are Cu. Cuprous oxide (A) forms a cubic lattice with a=4.27Å. Cupric oxide (B) forms a monoclinic crystal structure with a=4.68 Å, b=3.42 Å c=5.13 Å, and β=99.6°.
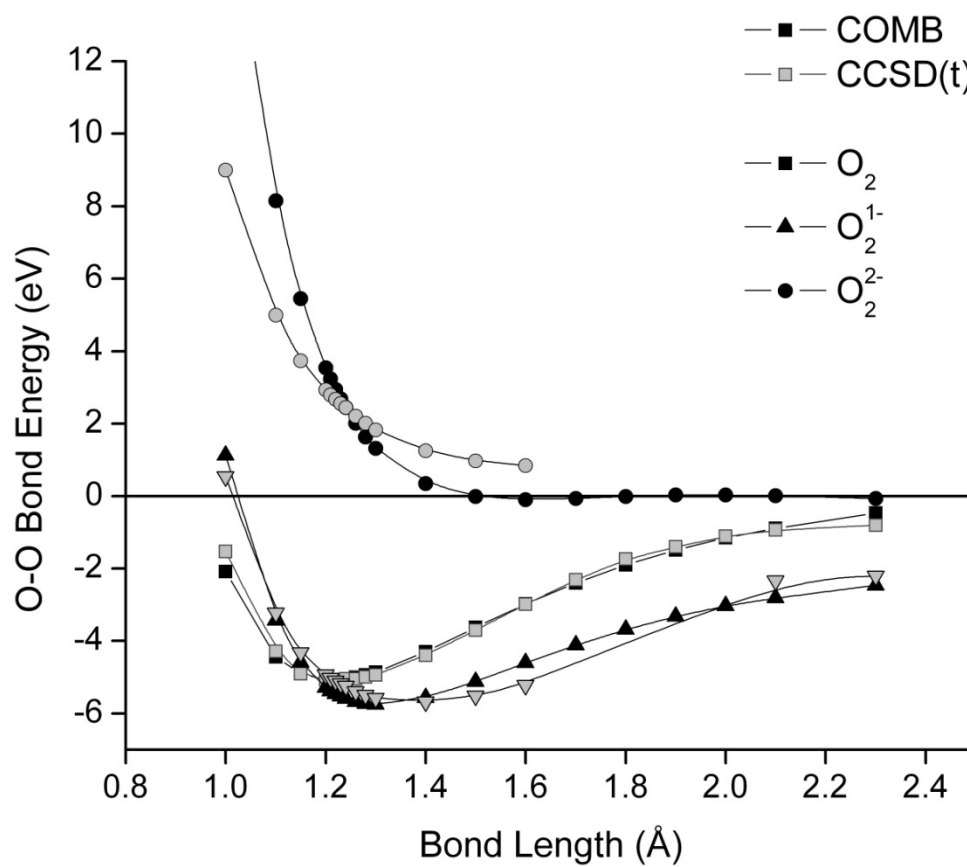
Figure 2. The bond dissociation energy of O_2 anions: Black symbols are values from the potential fit. Grey symbols are calculated (CCSD(t)/cc-pVTZ).
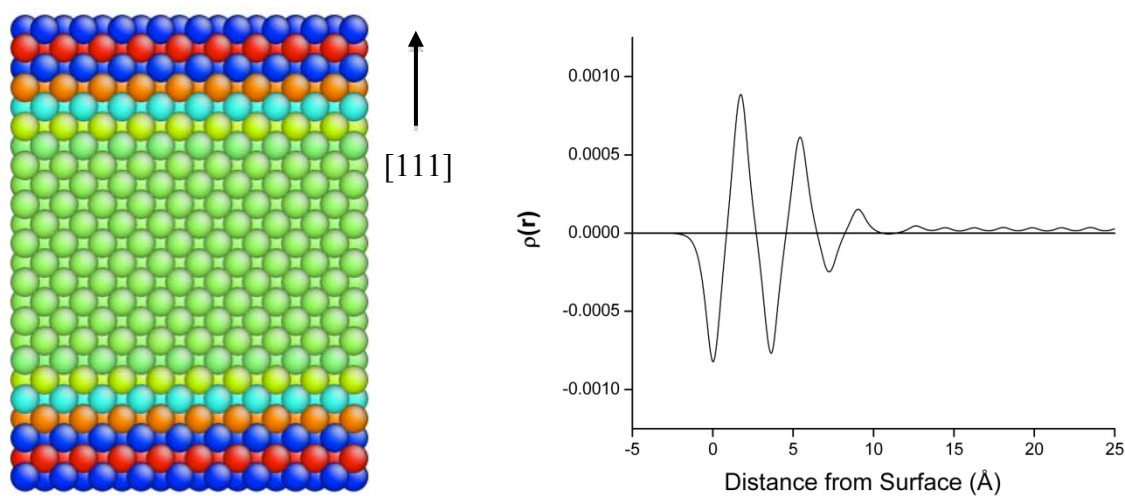
Figure 3. Surface charge in metallic copper. The copper surface exhibits negative charge The charge normal to the (100) plane is shown. Color corresponds to charge with blue=-0.1 and red-0.1 charge units. The plot shows the planar charge density distribution normal to the (100) surface.
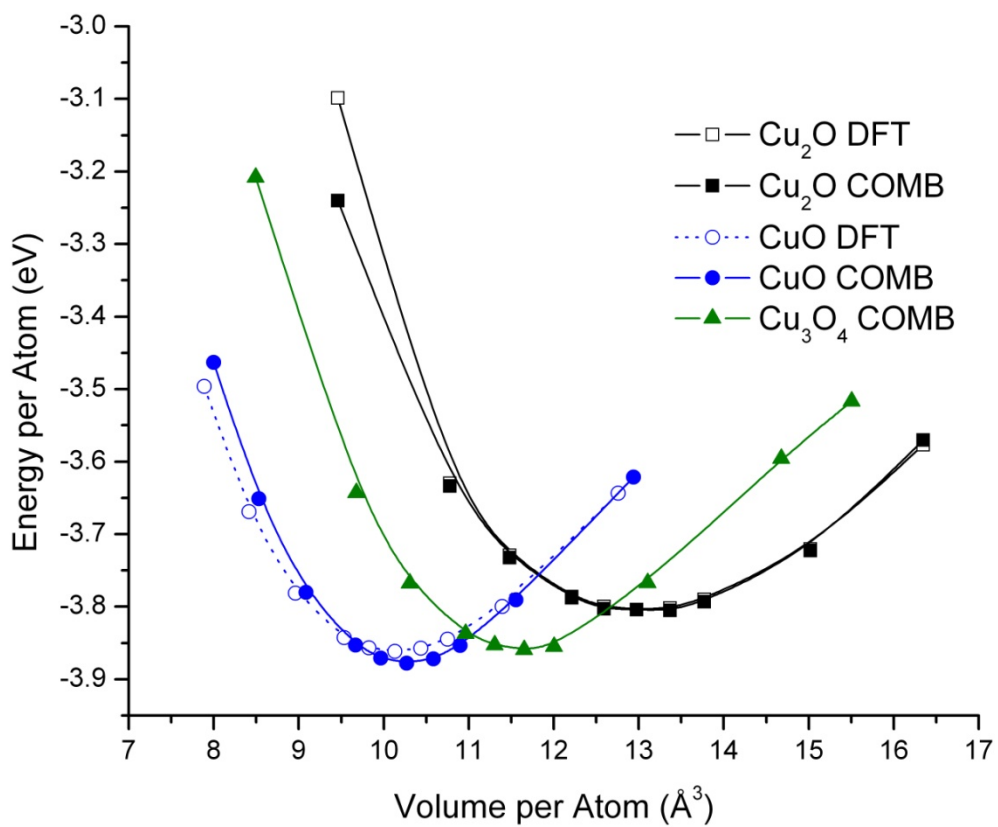
Figure 4.The energy per unit volume of the three low energy phases of copper oxide. Filled symbols represent COMB predicted values. Open symbols represent DFT values.

(a)
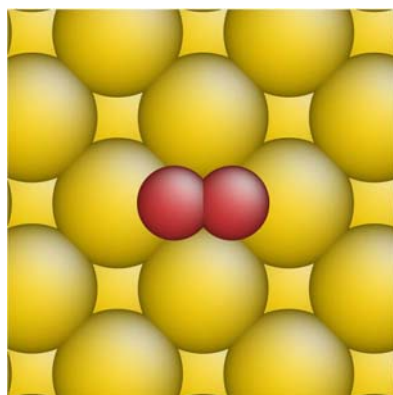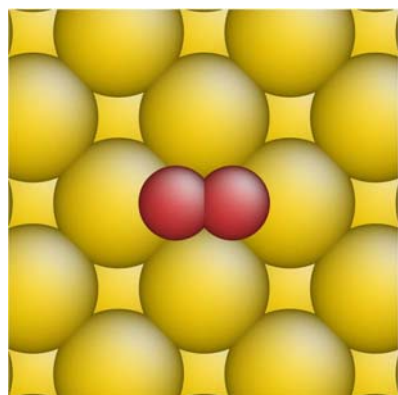
(b)
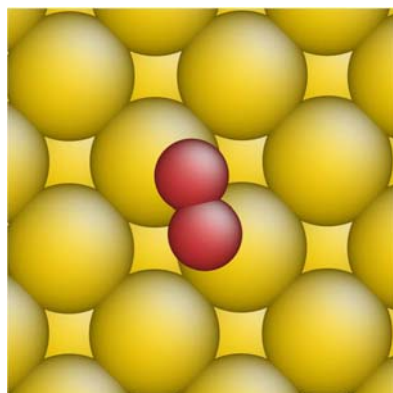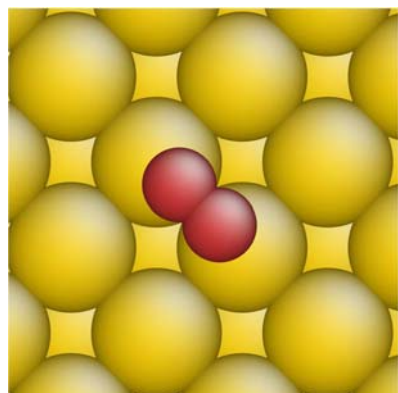
(c)
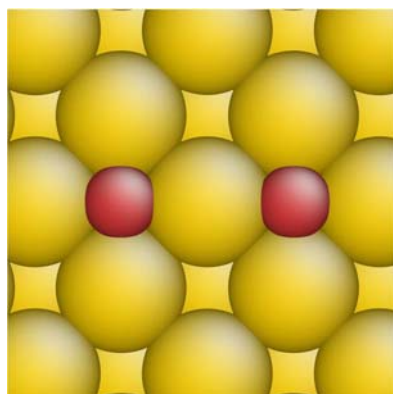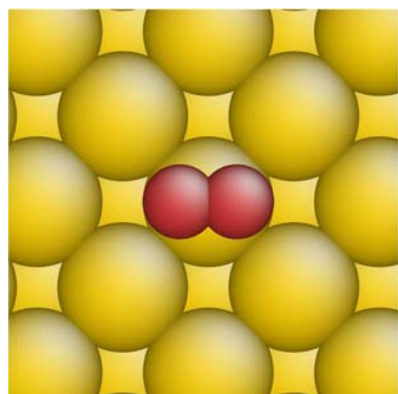
(d)
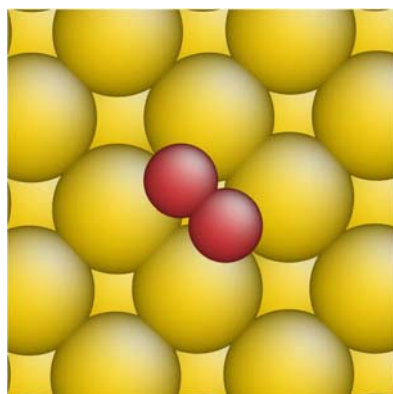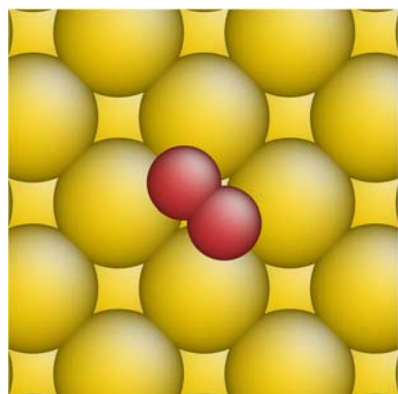
(e)
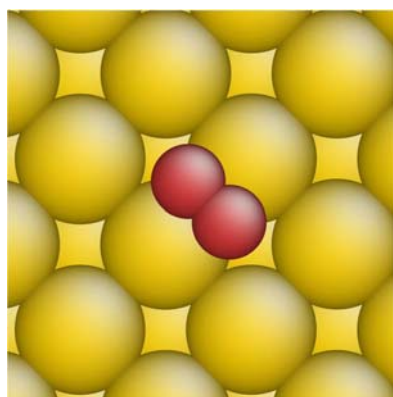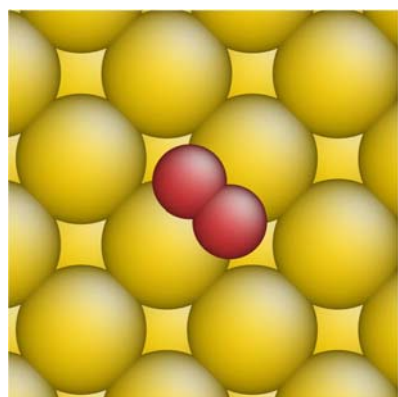
(f)
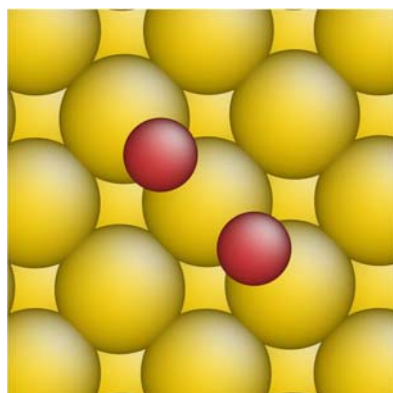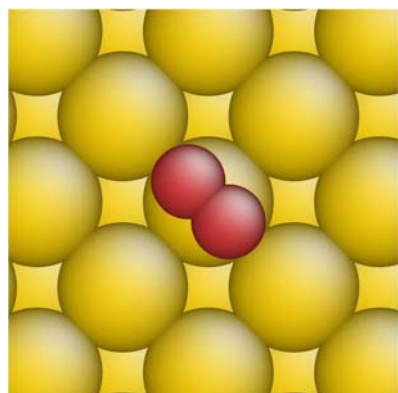
Figure 5. O_2 is placed on the Cu(100) surface in six orientations (a) Hollow site 1, (b) Bridge site 1, (c) Top site 1, (d) Hollow site 2, (e) Bridge site 2 and (f) Top site 2 relaxed using the COMB potential. The initial and final geometries are shown to the left and right, respectively. The small red spheres represent O and the large yellow ones are Cu. Initial orientations are 1.8 Å above the metal surface, final heights are given in Table 10.
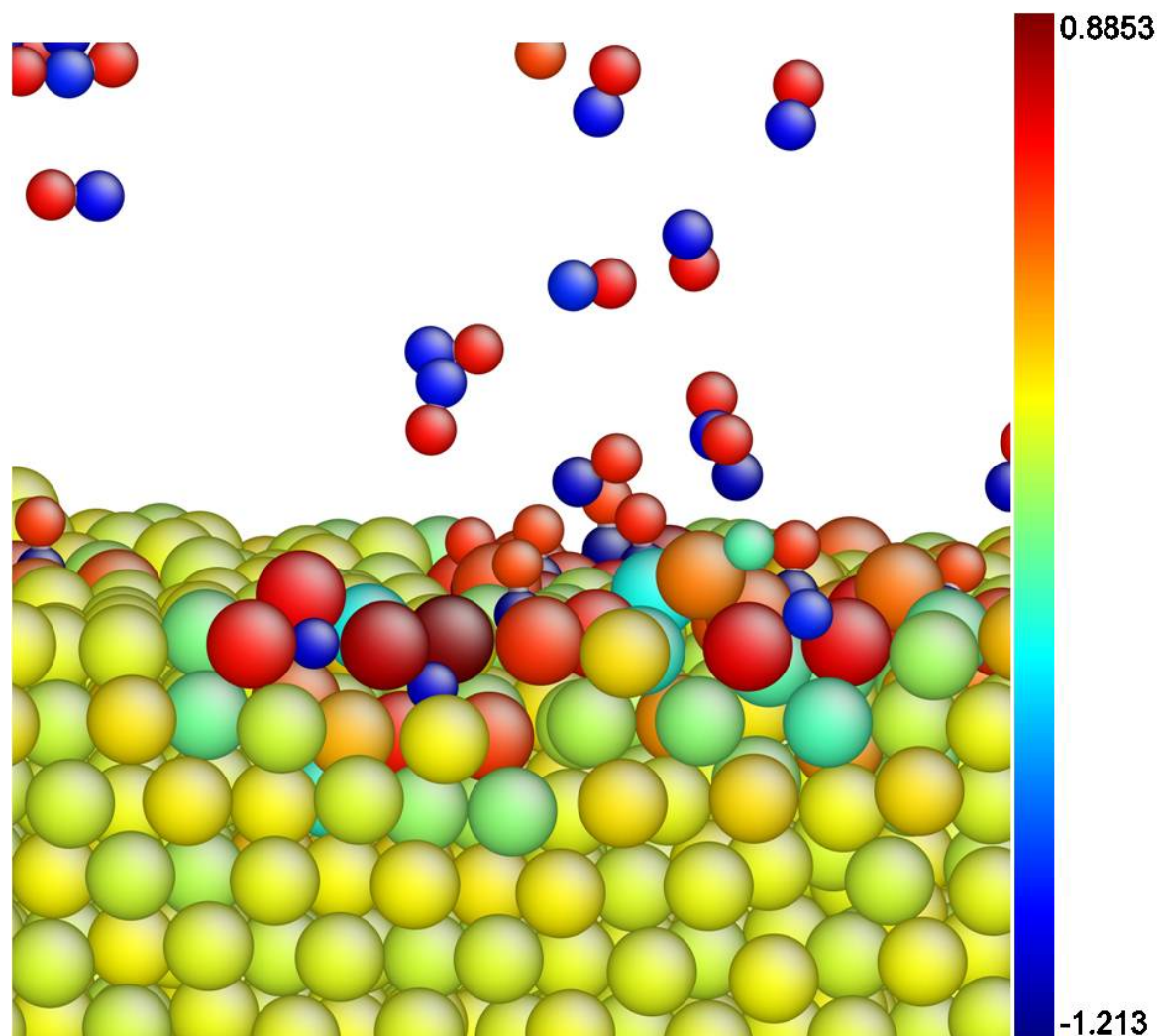
(a)
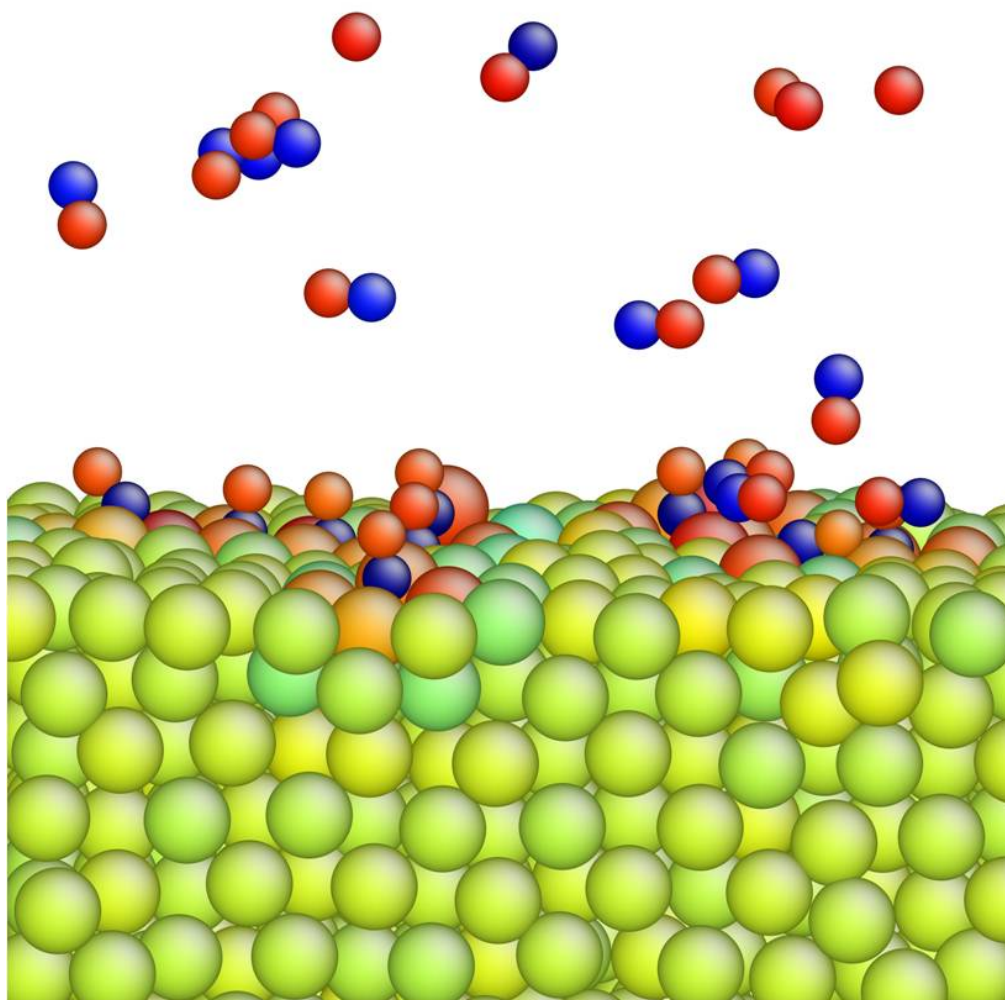
(b)

Figure 6. Oxygen molecules on clean Cu (100) surface at 1000 K, (a) after 1 ps, and (b) after 3 ps. Larger spheres are Cu, and smaller ones are O. The color corresponds to charge with red = 0.89e and blue =-1.21e.
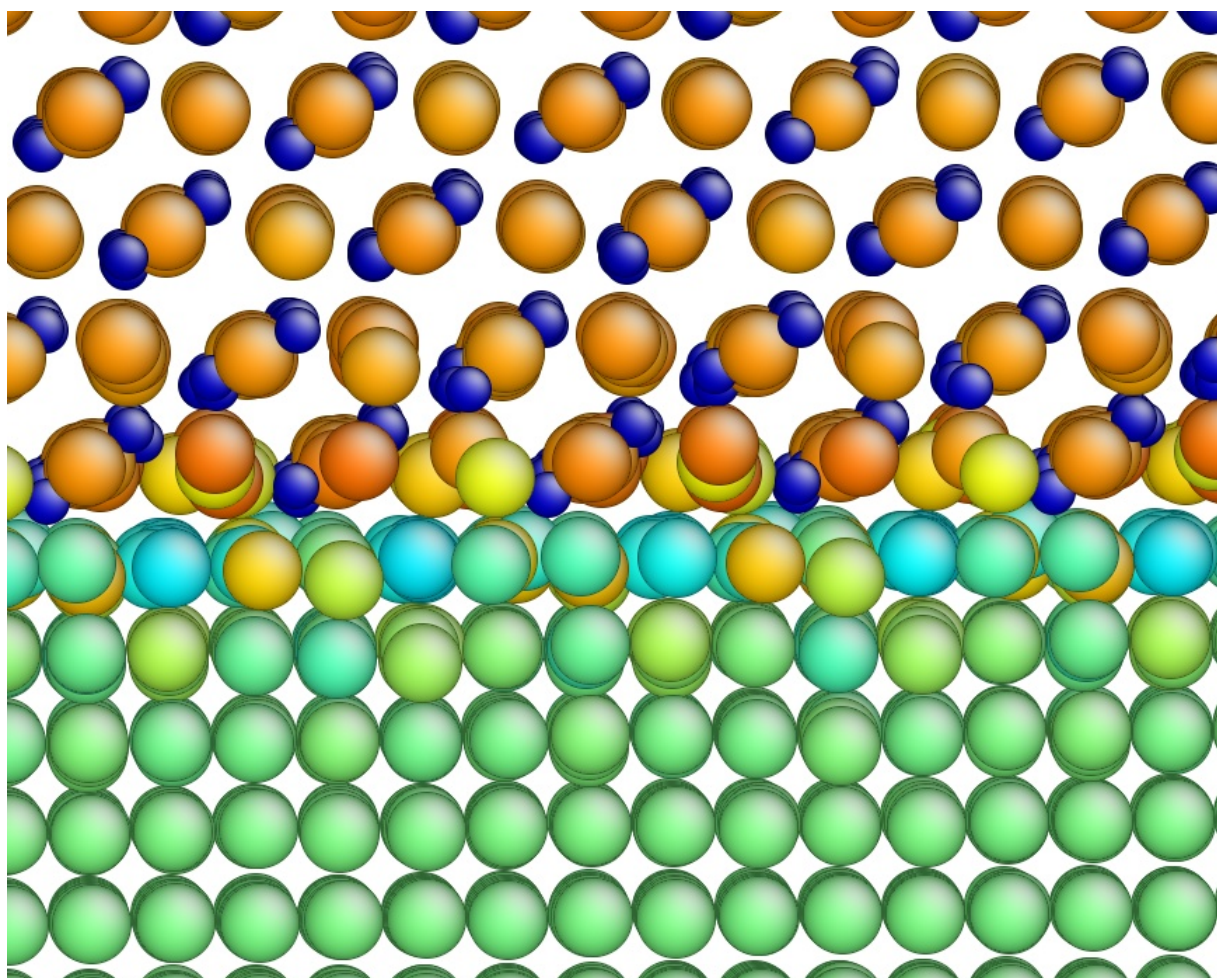
Figure 7. The $Cu_2O(111)||Cu(100)$ interface viewed along the Cu[100] direction after annealing at 200 K for 10 ps. Color corresponds to charge with red = -1.3 e and blue =1.3 e. The larger spheres are Cu. The smaller spheres are O. The interfacial region where the lattices are disrupted is confined to the first Cu layer in the oxide and one to two layers in the metal.
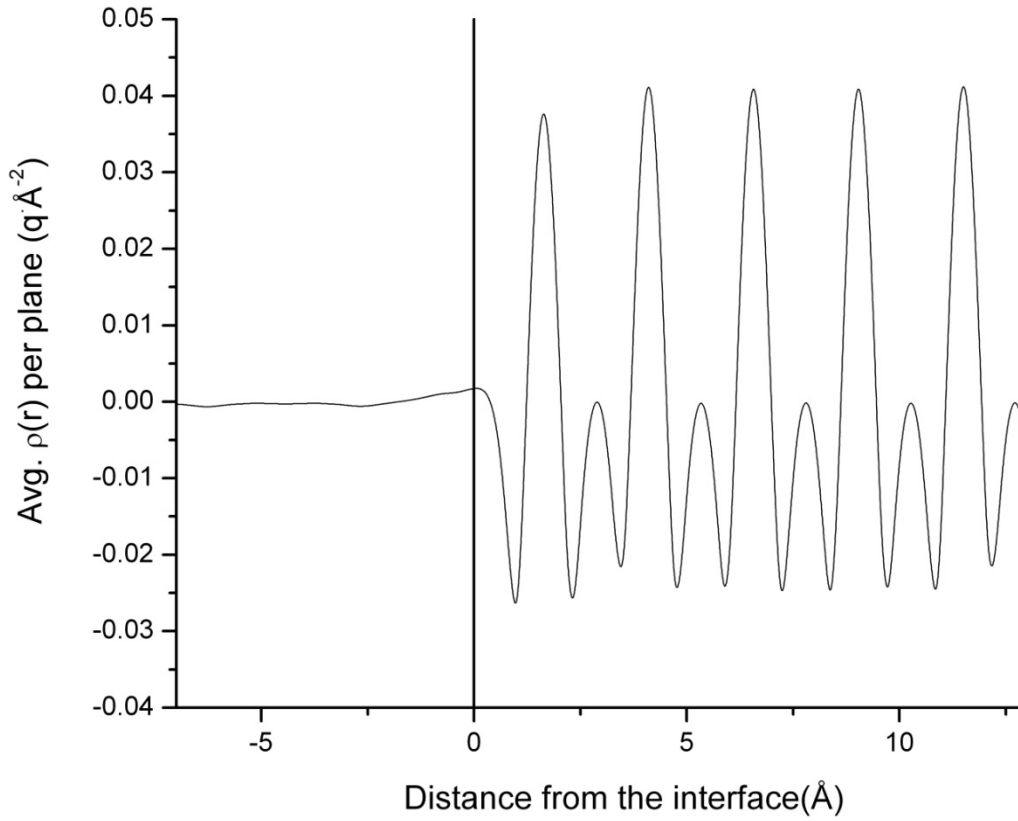
Figure 8.Planar average charge density across $Cu_2O(111)||Cu(100)$ interface after annealing at 200 K for 10 ps. Values are calculated per atom giving the average charge density per atom in each plane parallel to the interface. The zero point in the graph corresponds to the original interface. The oxide phase in on the positive side of the zero point. There is a slight charge transfer between phases at the interface, which is limited to the first 2 planes in each phase. Charge varies slightly around zero in the metal.